Correspondence to:
J. D. Carmichael,
josh.carmichael@gmail.com

Seismicity on the western Greenland Ice Sheet: Surface fracture in the vicinity of active moulins

Joshua D. Carmichael[1,2], Ian Joughin[1], Mark D. Behn[1], Sarah Das[3], Matt A. King[4], Laura Stevens[3], and Dan Lizarralde[3]

[1]Applied Physics Laboratory, Polar Science Center, University of Washington, Seattle, Washington, USA, [2]Geophysics (EES-17, GNDD), Los Alamos National Laboratory, Los Alamos, New Mexico, USA, [3]Department of Geology and Geophysics, Woods Hole Oceanographic Institution, Woods Hole, Massachusetts, USA, [4]School of Land and Food, University of Tasmania, Hobart, Tasmania, Australia

Abstract We analyzed geophone and GPS measurements collected within the ablation zone of the western Greenland Ice Sheet during a ~35 day period of the 2011 melt season to study changes in ice deformation before, during, and after a supraglacial lake drainage event. During rapid lake drainage, ice flow speeds increased to ~400% of winter values, and icequake activity peaked. At times >7 days after drainage, this seismicity developed variability over both diurnal and longer periods (~10 days), while coincident ice speeds fell to ~150% of winter values and showed nightly peaks in spatial variability. Approximately 95% of all detected seismicity in the lake basin and its immediate vicinity was triggered by fracture propagation within near-surface ice (<330 m deep) that generated Rayleigh waves. Icequakes occurring before and during drainage frequently were collocated with the down flow (west) end of the primary hydrofracture through which the lake drained but shifted farther west and outside the lake basin after the drainage. We interpret these results to reveal vertical hydrofracture opening and local uplift during the drainage, followed by enhanced seismicity and ice flow on the downstream side of the lake basin. This region collocates with interferometric synthetic aperture radar-measured speedup in previous years and could reflect the migration path of the meltwater supplied to the bed by the lake. The diurnal seismic signal can be associated with nightly reductions in surface melt input that increase effective basal pressure and traction, thereby promoting elevated strain in the surficial ice.

1. Introduction

Supraglacial lakes on the western margin of the Greenland Ice Sheet often drain by hydrofracture, thereby establishing pathways, known as moulins, for surface meltwater to reach the ice bed interface and influence basal motion [*Das et al.*, 2008; *Joughin et al.*, 2013; *Krawczynski et al.*, 2009; *Selmes et al.*, 2011; *Bougamont et al.*, 2014; *Tedesco et al.*, 2013]. Some observations suggest that basal hydrology of the Greenland Ice Sheet is qualitatively similar to that of mountain glaciers, where sliding is driven by changes in subglacial water storage and pressure provided by melt input through these moulins [e.g., *Bartholomew et al.*, 2011a, 2011b; *Shepherd et al.*, 2009]. Other evidence supports a model in which sliding variability is controlled by melt input only over diurnal and multiday scales [*Andrews et al.*, 2014; *Ryser et al.*, 2014]. In this case, longer-period changes in basal motion are driven by changes in connectivity between channelized and unchannelized portions of the bed rather than by the ability of moulin-connected subglacial channels to convey surface meltwater, particularly in the latter portion of the melt season (day of year or DOY > 210). This resilience to surface-delivered meltwater by the current distribution of draining lakes on the Greenland Ice Sheet can also be attributed to a layer of water-saturated basal sediments, or till [*Bougamont et al.*, 2014]. This model additionally predicts that ice speedup is more sensitive to higher-frequency discharge events earlier in the year, before drainage over bed sediments stabilizes. Because most documented fast (hour-scale) lake drainage events often occur during early to midsummer between DOY 180 and 210 [*Selmes et al.*, 2011], earlier lake formation may therefore exercise more transient influence on basal sliding prior to late summer changes in basal hydraulic connectivity, or till response. Recent analyses also suggest that the spatial distribution and timing of draining lakes have evolved over the previous two decades [*Liang et al.*, 2012] and that these lakes will likely advance inland with climate warming [*Leeson et al.*, 2015]. Changes in spatial moulin density and surface-to-bed connectivity in a warming

climate may play an important role in future ice dynamics of the Greenland Ice Sheet [*Fitzpatrick et al.*, 2014; *Doyle et al.*, 2014; *Bougamont et al.*, 2014]. Such changes, however, may be limited to lower elevations where surface crevassing is prevalent [*Poinar et al.*, 2015]. In particular, the appearance of lake-initiated surface-to-bed hydrological connections earlier in the season could trigger a sustained speedup by lowering effective basal pressures or, alternatively, could reduce average summer speedup by accelerating development of an efficient drainage network [*Sundal et al.*, 2009; *Schoof*, 2010]. It is therefore important to determine when, where, and how moulins form on the ice sheet. Often, such conduits form during brittle deformation events that accompany hydrofracture or extensional ice flow (e.g., crevassing) and thereby release seismic radiation through icequakes [*Stuart et al.*, 2005; *Carmichael et al.*, 2012]. Melt delivered to hard glacial beds by moulins may also induce basal icequakes through stick-slip or shearing motion that accompanies such sliding [*Walter et al.*, 2008; *Helmstetter et al.*, 2015]. If sliding motion is instead controlled by deformation of saturated till, basal icequake seismicity may be relatively quiescent. These competing models suggest that the creation and mechanical response to meltwater forcing in the lake-forming region of the Greenland Ice Sheet can be identified from the location and timing of surface icequakes, basal icequakes, or both. Coincident GPS measurements should then determine the extent to which this seismicity correlates with season variations in ice surface speeds and, ostensibly, ice flow.

Here we present seismic and geophysical observations collected over the 2011 melt season near a supraglacial lake southeast of Jakobshavn Isbræ that has drained each summer since observations began in 2006 [*Das et al.*, 2008, 2011]. These data capture rapid lake drainage and include several weeks of ice sheet response following the event that is coincident with transient changes in ice flow and seismicity. In particular, we analyze and interpret Rayleigh waveforms generated by located shallow-ice fractures near the drainage moulin and place bounds on detectable changes in seismicity induced by surficial and basal sources. Our study thereby advances current understanding of flow dynamics near draining supraglacial lakes on the Greenland Ice Sheet.

1.1. Background

Ice sheet response to meltwater forcing has been monitored using GPS [e.g., *Das et al.*, 2008; *Hoffman et al.*, 2011] and other remote sensing methods that measure ice flow over time [e.g., *Joughin et al.*, 2008, 2013; *Palmer et al.*, 2011]. Seismic methods also have been used to observe the effects of melt-triggered ice deformation by detecting and measuring the elastic energy released by processes such as hydrofracturing and basal sliding. In particular, several recent ground-based experiments in the lake zone of western Greenland also included seismic networks [*Das et al.*, 2008; *Doyle et al.*, 2013; *Jones et al.*, 2013; *Röösli et al.*, 2014]. These experiments have demonstrated that elevated seismicity accompanies hydrofracture of ice during lake drainage [*Das et al.*, 2008] and tectonic faulting of the ice sheet column during subsequent hydraulic jacking [*Doyle et al.*, 2013]. In these cases, additional icequake interpretation was limited by inadequate station coverage or a capability to associate waveforms on distinct geophones. Later work identified icequakes triggered by crevassing and moulin resonance under water input using a dense network of surface and borehole seismometers deployed in the ablation zone [*Röösli et al.*, 2014]. Similar experiments that involve alpine and polar glaciers have used seismic network data to detect and locate sources of icequakes triggered by meltwater [*Canassy et al.*, 2012; *Carmichael et al.*, 2012; *Mikesell et al.*, 2012; *Stuart et al.*, 2005; *Walter et al.*, 2008]. Some of these icequakes have been associated with basal stick-slip [*Thelen et al.*, 2013; *Allstadt and Malone*, 2014; *Helmstetter et al.*, 2015] or basal fracturing during subglacial cavity collapse [*Walter et al.*, 2009]. Other icequakes appear to be associated with shallow processes like brittle deformation of near-surface ice where high tensile stresses develop during meltwater-activated basal sliding [*Pomeroy et al.*, 2013; *Roux et al.*, 2010]. On the Greenland Ice Sheet, it remains unclear which among these processes produces icequake activity, since few experiments so far have been capable of distinguishing surficial from deeper seismicity [e.g., *Röösli et al.*, 2014]. In particular, the extent to which ice sliding over the bed produces basal seismicity remains unknown. Therefore, it is important to establish (1) when and where icequakes are triggered during a melt season in moulin-forming regions of the ice sheet and (2) whether icequakes are an indicator of ice sheet response to hydrological or other forcing, through changes in timing, location, or magnitude of the seismicity following drainage.
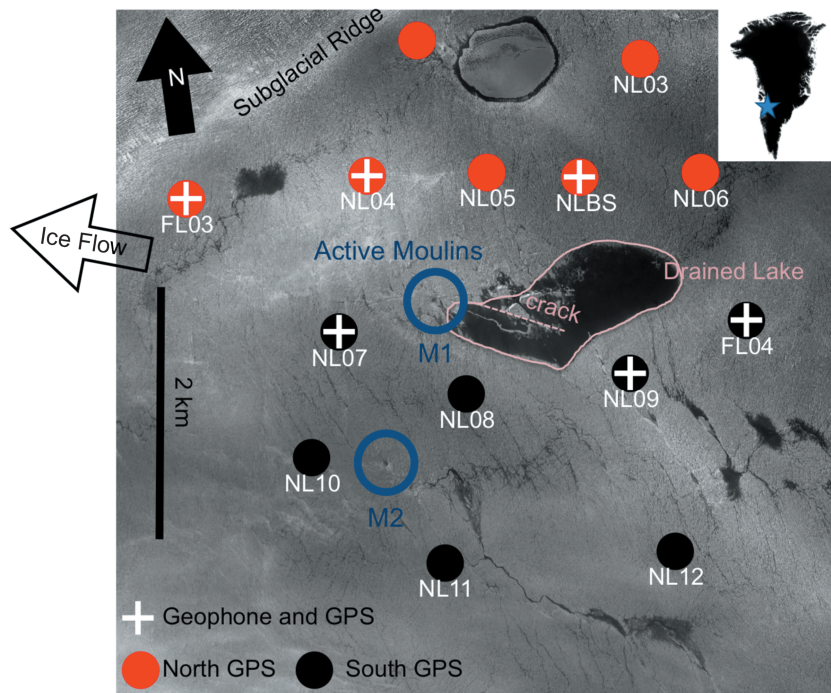
Figure 1. WorldView-2 image from DOY 168 showing the field site location (68.73°N, 49.53°W) in a region where supraglacial lakes form in Greenland's ablation zone. The outlined central dark region in the image center indicates the filled supraglacial lake shortly before drainage along with an older drainage fracture. GPS sites where Trimble GPS receivers were deployed in June 2011 are shown by filled circles. Crosses show locations of the six L-28, 4.5 Hz geophones that were paired with the GPS stations. Red and black markers respectively indicate sites north and south of FL03. Blue circle M1 shows the moulin that formed following the lake drainage on DOY 169, and M2 shows a nearby moulin that appears to have been active prior to the lake drainage.

2. Study Region and Instrumentation

Our field location, illustrated in Figure 1, was established in 2006 to study the effects of supraglacial lake drainage on ice deformation and regional flow [*Das et al.*, 2008; *Joughin et al.*, 2008]. From 2006 to midsummer 2014, geophones, temperature loggers, and GPS receivers were redeployed each summer in various configurations around the lake basin. Ablation rates at this elevation (~1050 m) are ~2 m a^{-1}, and ice thickness is ~980 m. Stresses in the lake basin are generally compressive due to flow convergence over a bedrock depression and become tensile west and northwest of the lake shoreline where the ice thins by a few hundred meters as it flows over a subglacial ridge (Figure 1). Ice flows west-northwest (~280°), with mean annual flow rates of ~80 m a^{-1} (~22 cm d^{-1}).

In mid-June 2011, the lake perimeter was instrumented with 6 Program for Array Seismic Studies of the Continental Lithosphere-supplied geophones, 18 University NAVSTAR Consortium-supplied GPS receivers, and an air-temperature logger. Each geophone site was collocated with a GPS station and included a three-component, 4.5 Hz, L-28 geophone and a Quanterra Q330 digitizer sampling at 200 Hz, logging to a hard drive. All geophones were mounted on identical pole platform assemblies, which were installed in ~2 m deep ice holes that were back filled with ice chips. One of these sites, NLBS, is a semipermanent "base station" that has collected GPS and seismic data near the field camp since 2006 and 2007, respectively. Each GPS site consisted of a Trimble NetRS or NetR9 unit sampling at 1 s intervals. Both the GPS and geophone data were time-stamped using coordinate universal time (UTC) and recovered in June 2012. Here we focus primarily on analysis of the seismic data.

3. Methods

The lake in Figure 1 drained on DOY 169 (18 June 2011) while the instruments were still being installed, so that only a partially deployed network (temporal coverage indicated in Figure 2) was logging data during
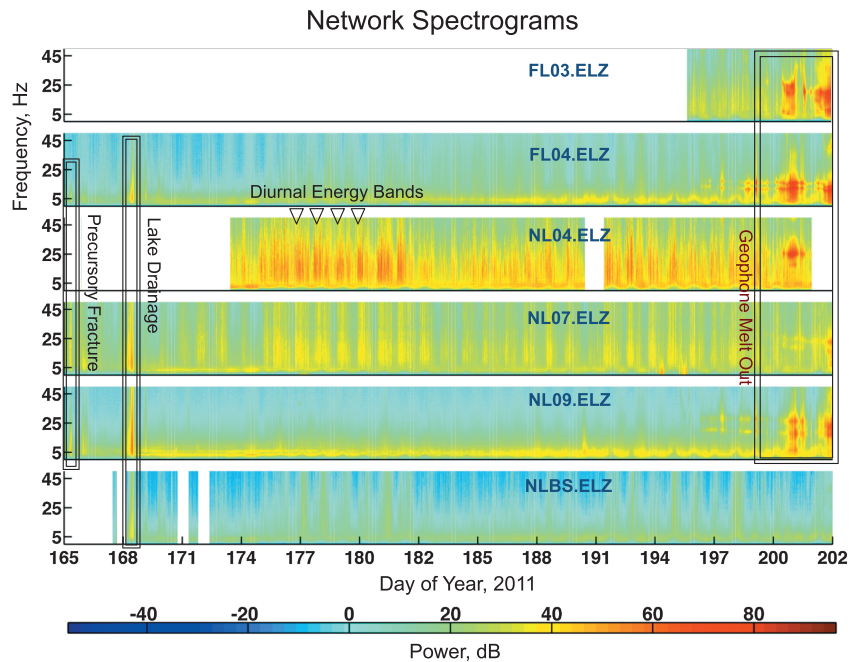
Figure 2. Band-limited spectrograms computed using the vertical component of available geophone data, indicated by station name and standard seismological short-period channel code ELZ. The color bar at the bottom indicates the range of signal power in decibels (dB). White regions indicate where only a partial geophone network was logging data. Features documented on this plot include elevated seismicity preceding hydrofracture, seismicity coincident with lake drainage, diurnal bands of elevated energy, and spectral curves indicating resonance caused by instrument melt out. All data refer to local time.

the event. Within ~12 h after drainage, we conducted an aerial survey by helicopter over the lake basin to document surface expressions of hydrofracture, including moulin and fracture locations. From these surveys, we determined that the hydrofracture opened a crack at least several hundred meters long, which appeared to have initiated near a moulin (M1 in Figure 1) that formed during the previous summer. This crack opened along a remnant high-angle hydrofracture-formed scarp at the lake bottom that was associated with prior drainages [*Das et al.*, 2008].

Our analyses in the following subsections include the data preceding, during, and several weeks following this lake drainage when the full array was installed. In section 3.1, we describe robust detection statistics used to quantify icequake emission rates and temporal trends in seismic activity, which are detailed in Appendix A. In section 3.2, we locate a subset of these icequakes using a novel beamforming method that also provides estimates of seismic attenuation factors. We further use these locations in section 3.3 to compute seismic magnitudes, hypocentral deformation volumes, and independent, secondary estimates for attenuation factors. In section 3.4, we measure relative changes in these icequake magnitudes over time by implementing multichannel cross-correlation methods. Finally, we process the GPS data in section 3.5 to compare time series of ice surface uplift and speed with seismicity.

3.1. Icequake Timing and Statistics

We identified individual icequakes by processing data from the vertical channel of each geophone using a noise-adaptive digital power detector. This detector computes a data statistic at each point in a geophone data stream by dividing an estimate of the sample variance within a leading data window by an estimate of the sample variance within a longer, following window, that is, the STA/LTA [*Blandford*, 1974]. To account for statistically correlated background noise, we computed robust estimates for the degree-of-freedom parameters of the data statistic's F distribution within each detection window (see Appendix A). These updated parameters enabled us to dynamically adjust the detector's event declaration threshold within each window and maintain a constant, acceptably low false-detection probability. We set this

probability to 10^{-6} using the Neyman-Pearson decision rule [*Kay*, 1998, Chapter 7], so that waveforms with a signal-to-noise ratio (SNR) of ~10 dB had a 95% probability of being detected on a single geophone in average noise conditions. Waveforms then detected on different geophones within a time interval less than the expected transit time of a shear wave across the network were identified as the same icequake (i.e., we performed waveform association). From these detections, we counted events that were large enough to be associated on three or more geophones and binned this count each hour to measure icequake seismicity. To quantify our confidence in this estimate, we identified time windows where the predicted null (signal-absent) F distributional curve for the STA/LTA statistic matched the data statistic's histogram with ≤20% root-mean-square error (see Appendix A). These signals provided our best hourly estimate of the seismicity as well as a measure of confidence in our estimates.

3.2. Hypocentral Distributions and Waveform Attenuation

The intrareceiver relative detection times for many of the seismic waveforms observed across our network suggest they emanated from local sources. Therefore, we used our geophone network to locate the largest of these icequakes that registered detections on three or more receivers. To obtain these locations, we computed double-difference travel time delays from an attenuation-compensating cross-correlation analysis developed for this study.

In applying this analysis, we first selected waveforms of predetected icequakes (section 3.2) by applying an automated quality control procedure that identified waveforms matching or exceeding SNR values of reference signals that were manually reviewed and labeled as acceptable for phase association. This produced ~435 icequakes with high-quality waveforms from a total of ~$3 \cdot 10^4$ events. We then prepared these data for our locating method by time reversing and reprocessing each waveform with the power detector to compute the signal end time. The data samples outside the (original) forward- and reverse-detected times were then muted (zero weighted) to eliminate noise exterior to the waveform interval. We next applied a frequency-dependent attenuation model [*Futterman*, 1962] in an attempt to correct for the individual propagation path effects from each waveform and to improve our estimate of cross-correlation time delays. These path effects were considered to result from attenuation and dispersion in the near-surface ice [*Gusmeroli et al.*, 2010; *Jones et al.*, 2013; *Peters et al.*, 2012], which caused a given icequake's waveforms to appear dissimilar on each geophone. We therefore processed the waveforms using a causal Futterman filter to model effects of anelastic attenuation and dispersion [*Pujol*, 2003, section 11.7] independent from geometric spreading. This filter has a frequency domain expression given by

$$A(\xi) = \exp(-\pi\xi t^*) \cdot \exp\left(-2\pi\xi t^* ln\left|\frac{\xi}{\xi_0}\right|\right) \tag{1}$$

Here ξ is frequency in Hertz, t^* is an attenuation parameter, and ξ_0 is the digitizer's Nyquist frequency (100 Hz). We computed filters for each detected icequake by numerically solving for the value of t^* (seismic wave travel time/seismic quality factor) in equation (1) that maximized the intrareceiver cross-coherency coefficient between the icequake's processed waveforms. Correlation-derived relative time delays between geophones were then compared with relative delays computed over a homogenous, 2 m resolution source grid. We used a wave speed of $c = 1670 \, \text{m s}^{-1}$ [*Mikesell et al.*, 2012] to compute these times after a visual inspection suggested that the processed data primarily consisted of Rayleigh waveforms (see section 4.2). Additionally, in order to account for ice sheet motion, we used the collocated GPS receivers to dynamically update our geophone locations over time. The grid search point that minimized the absolute sum of these time delay differences provided an estimate for each icequake's epicentral solution. Solutions exterior to the network, or with misfits exceeding 0.25 s, were regarded as too uncertain for reliable interpretation and were discarded. We estimated associated seismic quality factors (Q) from our located events by dividing the source-to-receiver travel time by the inverted value for t^* and averaging the results over the network.

3.3. Seismic Source Size and Waveform Attenuation

To gain additional insight into the mechanism for shallow-ice seismicity, we used relationships between seismic magnitude and source region size to estimate the deformation scale produced at each of the 435 located icequake's hypocenters. We assumed a crack-like seismic source model, based upon the apparent

dominance of Rayleigh waveform phases and visual evidence of surface fractures. The volumetric change δV caused by such a seismic source in confined media [*Aki and Richards*, 2002, p. 62] is given by

$$\delta V = \frac{M_0}{\lambda + 2\mu} \tag{2}$$

where λ and μ denote elastic Lamé parameters and $\lambda + 2\mu$ is the longitudinal modulus of the ice. δV is approximately related to the moment magnitude M_0 (dyn cm) through the surface wave magnitude M_S [*Mikesell et al.*, 2012]:

$$\log_{10}(M_0) \cong 1.5\,(M_S + 10.7) \quad \text{where:} \quad M_S = 1.5 \cdot \log_{10}\left(\frac{A}{T}\right) + F(R) \tag{3}$$

Here $\frac{A}{T}$ is the maximum Rayleigh wave amplitude-to-period ratio in microns per second, and $F(R)$ is the amplitude correction for a source-to-receiver distance of R. Volume change estimates like equation (2) sometimes include the bulk modulus $\lambda + \frac{2}{3}\mu$ instead [*Bowers and Hudson*, 1999], which refers to the stress-free volume change of a planar crack. We prefer equation (2), which gives the ice-confined volume change as a combination of the moment required to open a crack and to elastically push the surrounding ice away [*Müller*, 2001]. This "pushing" creates a displacement amplitude A_0 at the icequake source ($R = 0$) that is related to the geophone-recorded amplitude $A(R)$ by

$$A(R) = \left(\frac{A_0}{\sqrt{R}}\right) \exp\left(-\frac{\pi R}{cQT}\right) \tag{4}$$

where Q is the dimensionless surface wave seismic quality factor and c and T are the wave speed and period, respectively [*Mikesell et al.*, 2012].

To prepare the data for magnitude estimation, we deconvolved the instrument response of the L-28 geophone from the waveforms to obtain displacement records over [2.5, 40] Hz. Initial waveform amplitudes A_0 and attenuation factors π/cQT were then simultaneously inverted using a linear regression of equation (3), combined with equation (4). This regression extrapolated measured Rayleigh wave amplitudes to a zero epicentral distance where $F(R = 0) = 0$.

3.4. Relative Magnitude Analyses

To determine if repeatable icequake sources released increasing energy over time, thereby indicating enhanced ice deformation, we analyzed magnitude changes within icequake multiplets spatially localized to the same region. Such multiplets comprise clusters of variable-magnitude icequakes that reoccur as distinct seismic events, have similar hypocenters, and produce highly correlated seismograms [e.g., *Moriya et al.*, 2003]. We identified these events by computing the multichannel cross-correlation coefficients between waveforms from all 435 located icequakes. This coefficient generalizes the sample correlation between pairs of single-channel waveforms to pairs of multichannel waveforms, which represent measurements of seismic velocity recorded by a clock-synchronized geophone network [*Harris*, 1991; *Gibbons and Ringdal*, 2006]. Such a multichannel signal, sampled at interval Δt, is represented as a data matrix as follows:

$$W(t) = [w_1(t), \ldots, w_k(t), \ldots, w_N(t)], \quad \text{for } t = t_0, \ t_0 + \Delta t, \ \ldots, \ t_0 + N\Delta t \tag{5}$$

In equation (5), matrix column $w_k(t)$ is an N-sample seismogram from geophone k, recorded over T seconds from absolute reference time t_0 so that $w_k(t_0 + n\Delta t)$ refers to sample n from geophone k. The correlation coefficient $\rho_{1,2}$ that quantifies the similarity between two different multichannel signals $W^{(1)}(t)$ and $W^{(2)}(t)$, recorded from two different events, is derived from a maximum likelihood estimate [e.g., *Harris*, 1991; J. D. Carmichael et al., Detecting Weak Explosions at Local Distances by Fusing Multiple Geophysical Phenomenologies, *Geophysical Journal International*, in review, 2015], given by

$$\rho_{1,2} = \max_{\Delta t} \left\{ \frac{\text{tr}\left(W^{(1)}(t + \Delta t)^{\mathsf{T}} W^{(2)}(t)\right)}{\left\|W^{(1)}(t)\right\|_F \left\|W^{(2)}(t)\right\|_F} \right\}, \tag{6}$$

where $\|W^{(k)}(t)_F\|$ is the matrix Frobenius norm and $\text{tr}(W^{(k)}(t))$ is the matrix trace of $W^{(k)}(t)$ ($k = 1, 2$). When only a subset of network geophones was logging data in a given period, just those matrix columns containing

operational stations were compared. We thereby required three or more stations to be operational at any time and only included event pairs where $\rho \geq 0.5$ (subscripts omitted) for analyses after visual inspection suggested that waveforms sharing lower correlation likely had dissimilar sources. This correlation threshold gave a $\leq 10^{-6}$ false-attribution probability between each event pair, as determined by the correlation coefficient's empirical null distribution [e.g., *Weichecki-Vergara et al.*, 2001; *Carmichael*, 2013]. We then clustered the waveforms of located icequakes into groups based upon this correlation coefficient by using a complete linkage algorithm [*Carmichael et al.*, 2012; *Allstadt and Malone*, 2014]. The relative seismic magnitude ΔM of an event with data matrix $\boldsymbol{W}_1^{(2)}(t)$ in a given cluster, compared to a reference event with data matrix $\boldsymbol{W}_1^{(1)}(t)$, in that same cluster, is then given by [*Schaff and Richards*, 2014]

$$\Delta M = \log_{10}\left(\frac{\left\|\boldsymbol{W}^{(2)}(t)\right\|_{\boldsymbol{F}}}{\left\|\boldsymbol{W}^{(1)}(t)\right\|_{\boldsymbol{F}}}\right) \tag{7}$$

where the estimator bias due to correlation is removed and the reference event (index 1) is taken to be the earliest within the cluster. Equation (7) provides a more precise means for determining relative magnitudes when compared to methods based on differencing.

3.5. GPS Data Analysis

We processed the GPS data following the general approach of *King and Aoki* [2003]. First, we analyzed the raw carrier-phase and pseudorange GPS data within the GPS Inferred Positioning System/OASIS v6.1.2 software using a precise-point positioning strategy [*Zumberge et al.*, 1997] by applying uniform observation weighting and a satellite elevation cutoff angle of 10°. We then estimated station coordinates every 15 s as a white noise process, holding the high-rate Jet Propulsion Laboratory fiducial satellite orbit and clock values fixed, and estimated every measurement epoch's white noise receiver clock and random walk parameters associated with residual wet, tropospheric zenith delays and tropospheric gradients. For the tropospheric mapping function, we adopted the gridded Vienna Mapping Function 1 and computed a priori tropospheric zenith delays from European Centre for Medium-Range Weather Forecasts grids [*Boehm et al.*, 2006]. At the observation level, we modeled solid Earth tides [*Petit and Luzum*, 2010] and ocean tide loading displacements using Some Program for Ocean-Tide Loading [*Agnew*, 1997], as based on the TPXO7.2 ocean tide model [*Egbert et al.*, 2009]. Where possible, we fixed carrier-phase ambiguities to integer values [*Bertiger et al.*, 2010]. To minimize day boundary effects, we processed data in 30-h windows centered on midday and then truncated the time series back to UT days. We then rotated the final coordinate time series into a local north-east-up coordinate system for further analysis. Remaining outliers, at day boundaries and elsewhere, were visually identified from detrended data and then discarded. Finally, we computed surface velocities in each direction by differentiating positions that were presmoothed with a 12-h width, zero-phase Butterworth filter.

4. Results

We first present general seismic and GPS results without detailed reference to the lake drainage on DOY 169 (sections 4.1–4.6) and describe our cumulative geophysical observations preceding and following this drainage thereafter (sections 4.7 and 4.8). In section 4.1, we summarize icequake timing, statistics, and temporal variability. In section 4.2, we identify the dominant seismic Rayleigh phase and characterize its anelastic attenuation in the near-surface ice. To interpret the dominance of these waveforms, we then quantify observation bias favoring detection of surface versus basal icequakes in section 4.3. Next, we discuss the epicentral distribution, magnitude, and physical dimension of the sources producing the detected and located icequakes in section 4.4. We then analyze magnitudes of located events using a quantitative comparison of predrainage and postdrainage icequakes in section 4.5. In section 4.6, we detail GPS-derived ice surface motion histories, along with spatiotemporal averages of surface speed. Finally, we summarize these geophysical observations to describe the ice sheet response over time leading up to (section 4.7) and following (section 4.8) lake drainage.

4.1. General Icequake Timing and Statistics

Figure 2 shows a subset of the velocity amplitude spectra (spectrograms), computed from the vertical channel of each geophone. These spectrograms revealed several coincident time periods of elevated

seismicity measured across the network, which are indicated and labeled. We estimated network-averaged dominant frequencies of ~15 Hz during these periods, which are somewhat lower than the ~25 Hz values reported near our site during the 2010 melt season by others [*Jones et al.*, 2013]. These spectrograms also revealed strong harmonic signals that were visible starting at DOY ~200, decreased over time, and extended through the remainder of the melt season [*Carmichael*, 2013, Appendix C]. This is somewhat similar to the moulin resonance signal reported by *Röösli et al.* [2014]. However, an analysis of the resonance modes for the pole used to anchor the seismometer suggests that surface melting caused the geophone pole platforms to melt out, which induced a platform resonance [*Carmichael*, 2013] that resulted in the harmonic signal. This interpretation is supported by similar observations from a 2009 experiment conducted at the same field site. Specifically, in 2009, similar signals coincident with instrument melt out disappeared after site maintenance and fresh installation of the seismometers. Thus, we truncated our analysis to frequencies ≤50 Hz, where energy from seismic waveforms was expected to remain more spatially coherent across the network and limited our study period from days 165 to 200, when resonance from melt out was absent or minimal. It is unlikely that the removal of these higher-frequency signals resulted in a significant loss in detections. We estimated that icequake sources producing substantial spectral energy at or above 50 Hz would have source dimensions ($<2\,m^2$) [*Gibowicz and Kijko*, 1994, Equation (11.31)] and magnitudes (< -2) that would limit their probable observation to no more than one sensor. As a result, such events would not pass our three-station association rule.

Figure 3a illustrates the cumulative number of discrete icequakes detected per hour on three or more geophones, during this study period. This signal shows variability over at least two distinct periods. To better expose these dominant periods, we computed a spectrogram of the seismicity using ~1 day long windows with 90% overlap (Figure 3b). This spectrogram of icequake counts highlighted ~10 and ~12 day intervals of elevated diurnally variable activity, punctuated by intervals of lower amplitude activity. We evaluated dependencies in this seismicity on time of day by binning icequake counts by hour of the day and excluding times containing drainage-associated events (Figure 3c). The resulting histogram illustrated higher icequake detection rates in early morning hours, with minimum activity occurring near 18:00 local time. The 23:00 h bin likely underestimated true counts, as seismic data volumes were occasionally truncated before local time 23:30.

Because seismic noise often fluctuates over subdaily periods in glacial settings [e.g., *Walter et al.*, 2008], we also determined if the diurnal signal and histogram asymmetry in Figures 3a–3c could be produced from variable noise power, rather than by icequake activity. To do so, we estimated the influence of icequake waveform signal-to-noise ratio (SNR) on the performance of our adaptive STA/LTA detector (see section 3.1). This required computing hourly estimates of four processed noise parameters shaping the detection statistic's *F* distribution function (discussed in Appendix A). We then used these parameters to compute the threshold SNR required to achieve a 95% detection probability for each hour of each day (equations (A2)–(A4)). These threshold SNR values were then averaged into 24, hourly time-of-day bins for comparison with SNR averages computed from detected waveforms, using an unbiased SNR estimator [*Kubokawa et al.*, 1993]. The detected-waveform SNR averages consistently exceeded the respective threshold SNR by several decibels (Figure 3d). Thus, we conclude that the diurnal seismicity was produced by geophysical sources and not caused by changes in noise variance that suppressed or elevated detection rates.

4.2. General Seismic Phase Characteristics

To identify waveform phases, we visually reviewed ~5000 seismic record sections from a total of $3 \cdot 10^4$ events that triggered our power detector and were associated on three or more stations. These ~5000 events were randomly drawn from the detection population over a period spanning the recording period. Common features of these waveforms include ~1 s signal lengths, spectral energy peaks at ~15 Hz (in agreement with mean spectrogram peak energy), and displacement waveform wavelengths of ~330 m (computed from instrument deconvolved data). Waveforms from the same source often appeared dissimilar on distinct vertical geophone channels (Figure 4a, black signals) and only showed substantial coherence after attenuation modeling (Figure 4a, blue signals). This indicates that the glacial ice was dissipative over array aperture-scale propagation distances, with a seismic quality factor of $Q \sim 35$ at typical waveform frequencies (Figure 4b). Our analysis also revealed consistent apparent differential time lags present between the horizontal and vertical channels of the largest-amplitude and latest arriving
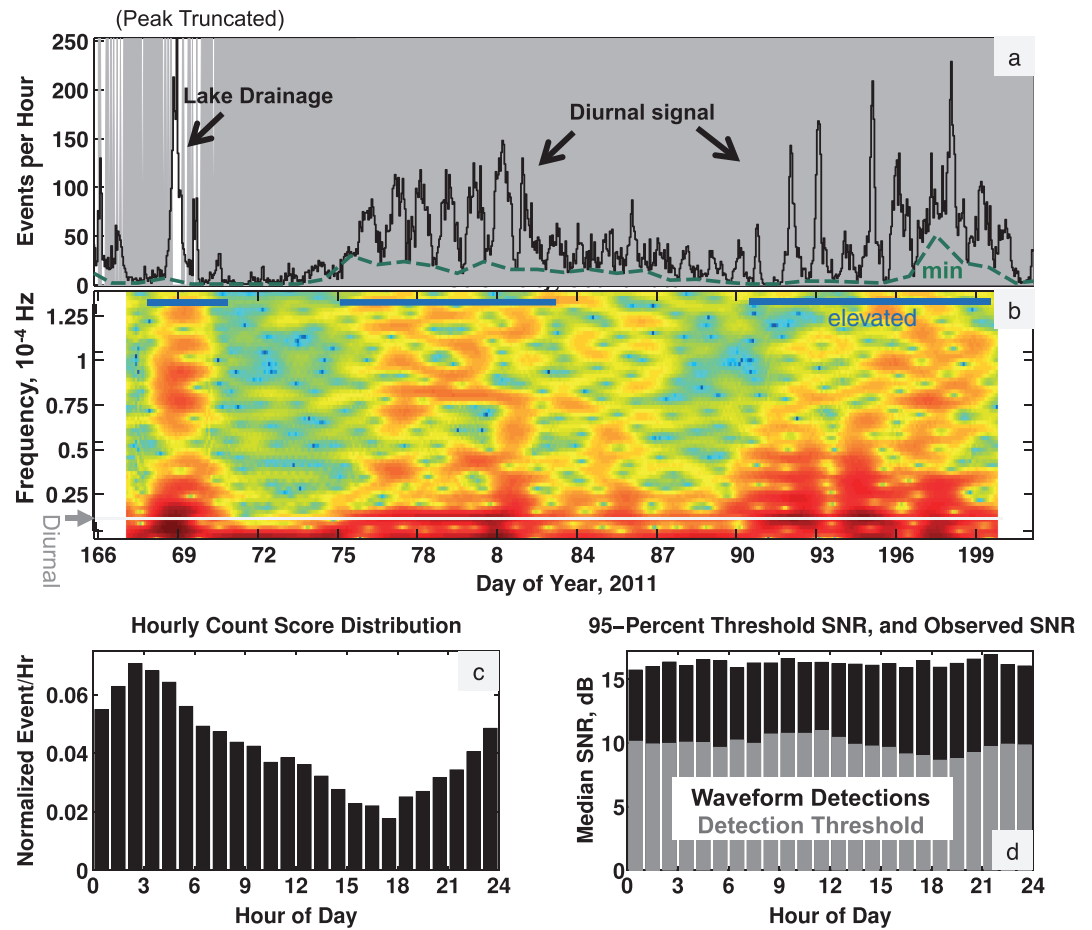
Figure 3. Summary of icequake seismicity and corresponding detection statistics. All dates indicate local time. (a) Number of icequakes detected per hour (seismicity) on any three or more operational geophones within the network, using an STA/LTA detector (Appendix A) including a 160-sample short-term window and 1000-sample long-term window. Peaks prior to and during drainage are labeled for reference, and the green dashed line labeled *min* indicates the minimal count rate in a day. The gray shading indicates bins where the STA/LTA detector statistic's predicted null distribution fit the observed distribution with less than 20% error. (b) Spectrogram of the seismicity in Figure 3a computed after subtracting the minimal daily count rate (green curve). The thin, gray horizontal line indicates the diurnal frequency component, and the blue bars labeled *elevated* indicate intervals of increased short-period variability. Blank portions of the spectrogram end points are due to spectral windowing. (c) Seismicity from Figure 3a binned by hour of day. Days preceding and during rapid lake drainage were removed from counting. (d) Median signal-to-noise ratios (SNR) computed from detected icequake waveforms (black) compared with the median, unbiased SNR thresholds required to achieve a 95% detection probability in each hour. This threshold SNR was conditional upon several noise statistics estimated within each detection window.

waveform phase for a given event (Figure 5a). To explore these lags, we phase advanced the vertical waveforms by 90° using a Hilbert transform and found that the resulting waveforms matched the horizontal components of motion (Figure 5b, red waveforms), indicating that the original signals were elliptically polarized [*Chael*, 1997]. We do not expect such lags to be present from body waves originating from deep sources beneath our array, or at the range of observed azimuths. Rather, these relative lags are characteristic of Rayleigh waves that originate from shallow or surficial sources and have non dip-slip focal mechanisms [*Aki and Richards*, 2002, p. 329]. Thus, we conclude the dominant source of detectable seismicity (95% by number of events) is due to shear or tensile surficial fracturing. By contrast, only a minority of waveforms (~5%) that we visually observed from our sample exhibit characteristics of pure body wave arrivals. Many from this minority population are attributable to sources external to the lake region based on their relative arrival times within the geophone network. Consequently, surficial sources produced most of the detected, local seismicity.
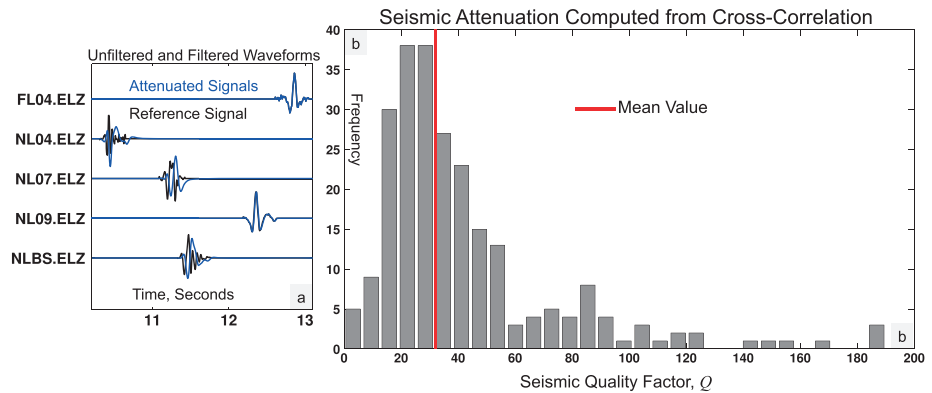
Figure 4. (a) Preprocessed and postprocessed vertical-velocity geophone waveforms used to locate icequakes. Original, recorded waveforms are shown in black. Blue waveforms are causally attenuated to maximally correlate with the latest arriving signal. In this case, the signal measured at FL04 comprised the last arrival and was consequently not processed with the attenuation filter. (b) Seismic quality factors (Q) estimated from inverted values of the attenuation parameter t^* that were obtained by maximizing cross-correlation coefficients between waveforms as show in Figure 4a. Nonphysical estimates (negative Q) were discarded. These values are in general agreement with attenuation factors computed elsewhere on the Greenland Ice Sheet near our site [*Peters et al.*, 2012], and with the estimates obtained independently in Figure 8b.

4.3. Surface Versus Basal Icequake Detectability

To assess the apparent lack of basal seismicity in our data, we used principles of seismic threshold monitoring [*Ringdal and Kværna*, 1992] to estimate surface and basal icequake magnitudes providing a prescribed detection probability at the longest-recording station (NL07, Figure 1). We first applied a simple seismic signal model that includes effects of the source radiation pattern, propagation path, free surface amplification, and instrument response on a hypothetical recorded waveform (Appendix B, equation (B1)). We then used the signal-present distribution function of the STA/LTA detection statistic computed by our power detector at each sample to invert for seismic signal amplitudes consistent with a 95% detection probability. This distribution function and its parametric arguments are summarized in Appendix A
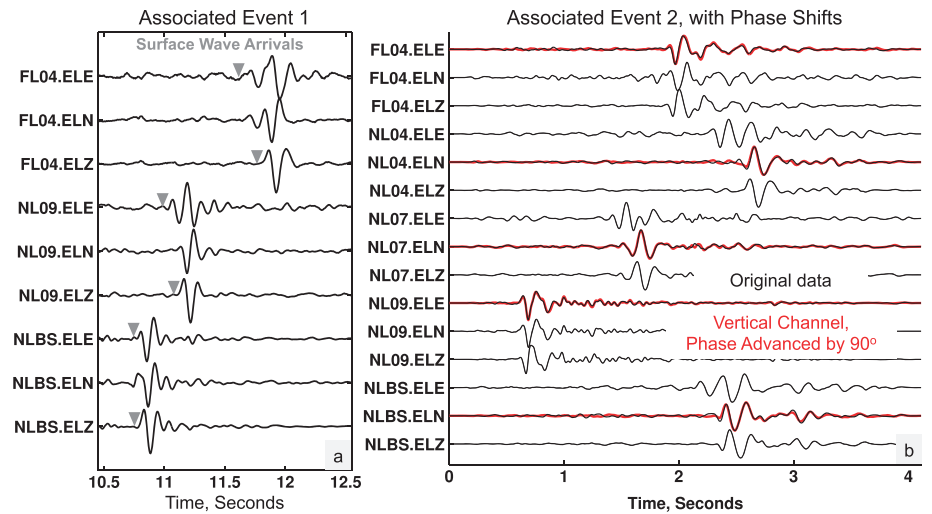

Figure 5. (a) A multichannel record section illustrating waveforms recorded on three of the six available geophones for a typical icequake. The gray markers indicate the differential time lags between the vertical and horizontal components of the dominant waveform phase. The icequake source is likely nearest to NLBS, where the phase lags are less pronounced. (b) A record section for a second event illustrating comparisons between the vertical and horizontal components of motion. Selected horizontal channels for each geophone are superimposed with 90° phase-advanced (Hilbert-transformed) vertical components to illustrate their strong linear correlation (shown in red). The phase similarity between the horizontal and phase-advanced vertical components suggests the original waveforms are elliptically polarized Rayleigh waves.
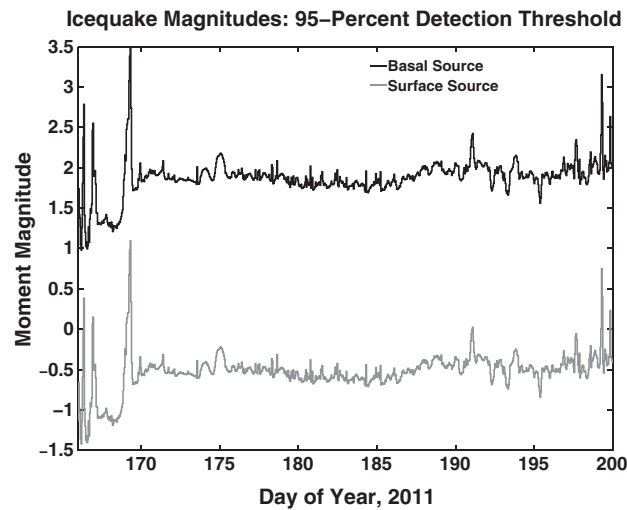
Figure 6. Single-phase threshold magnitudes for surficial and basal icequakes computed hourly over the study period (in local time). The black curve illustrates the greatest magnitude required of a hypothetical, pure shear wave source to trigger detections with <95% probability and 10^{-6} false alarm rate, using our power detector in the observed noise environment. The modeled source was located at the ice sheet bed, directly beneath the center of the geophone network in Figure 1. The gray curve shows the corresponding threshold magnitude required of a hypothetical, pure Rayleigh wave source for the same detection rates and located at the ice surface, in the center of the array. Additional waveform phases would likely reduce these threshold magnitudes.

(equations (A1)–(A5)). In brief, the first of these parameters, λ, is proportional to the (unknown) waveform SNR measured in the leading, length S detection window (equation (A2)), while the following two parameters shape the distributional curve and depend on the temporal correlation of the noise (equation (A4)). To estimate the waveform amplitude consistent with a 95% detection rate, we inverted for the threshold values of the SNR parameter ($\hat{\lambda}_{95}$) satisfying our false alarm constraint (equation (A5)). We then combined these hourly estimates of $\hat{\lambda}_{95}$ and the mean radiation pattern coefficients applicable to each source to compute threshold, scalar moment values specific to basal and surficial sources.

Our computations (Figure 6) demonstrate that hypothetical basal icequakes resulting from horizontal sliding are less likely to be detected in the measured noise environment relative to hypothetical surficial icequakes triggered by tensile or shear fracture opening.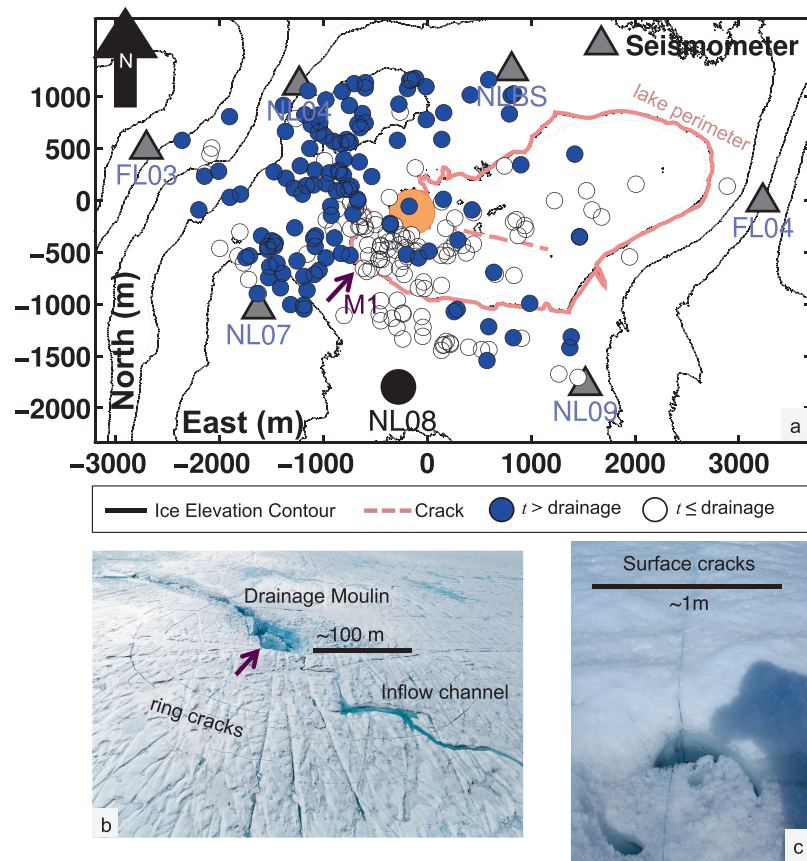 Under our simplified assumptions, a 95% detection probability requires a moment magnitude of $M_w \sim 1.9$ for basal sources in contrast to $M_w \sim -0.45$ for surficial sources, excluding drainage data. The peaks in threshold on DOY 169 are likely due to the unusually high seismic activity concurrent with lake drainage, which amplifies minimal detection thresholds and background noise [e.g., *Ringdal* and *Kværna*, 1992]. This suggests that detection methods with a higher discrimination capability than the STA/LTA are required for identifying basal icequakes of comparable magnitude to surface icequakes, such as network-based cross-correlation [*Harris*, 1989; *Gibbons and Ringdal*, 2006; J. D. Carmichael et al., unpublished data, 2015]. The curves in Figure 6 likely underestimate the true detection capability, since observed seismograms generally contain a higher-energy superposition of several phases (rather than shear and Rayleigh only) that would increase λ_{95} and thereby decrease threshold magnitudes.

4.4. Seismic Source Location and Size Distribution

Figure 7a illustrates the epicentral distribution of the 435 icequakes that we located in the lake basin and its immediate vicinity. Located events occurring before and up to 24 h after drainage (white) predominantly cluster on the upstream side of the lake basin, with a particularly high density of events located near the drainage crack tip and adjacent moulin, M1 (purple arrow, Figure 7b). Events occurring after drainage generally cluster northwest and downstream of these earlier icequakes (blue). While our locations include only a small fraction of all total events (435 of $\sim 10^4$ in number), they represent the largest observed icequakes (highest SNR) and are ostensibly the most significant observables of deformation. We refer to our results on the lake drainage timeline in sections 4.6 and 4.7 for additional details regarding predrainage versus postdrainage icequake epicenters.

The filtering and correlation operations included in our attenuation and relative time delay calculation method (section 3.2) made it difficult to quantify icequake location uncertainties. We therefore estimated errors empirically by computing epicentral distances between events within multiplets, under the assumption that repeating sources produced highly correlated waveforms (see section 3.4). To further restrict this calculation to icequakes most likely to collocate, we only compared events with cross-correlation coefficients ≥0.95. We thereby found a mean, epicentral distance of 124 m among 23

Figure 7. Summary of the icequake locations. (a) Epicenters of 435 icequakes plotted over a surface elevation contour map. These were selected from ~3·10⁴ total icequakes by requiring events to have pick times from at least three geophones and high enough SNR at all stations for reliable waveform identification and thus locating. Events detected before and up to 24 h after drainage (local time) are shown in white. Events detected later are shown in blue. The orange circle shows the one standard deviation uncertainty circle, centered at the drainage crack tip, and the purple arrow refers to the drainage moulin M1 in Figure 1 (M2 is outside axis range). The local coordinate system origin coincides with the geophone network center. (b) The lake drainage moulin (~50 m wide) viewed from air. Labeled features include circumferential fractures that likely developed due to subsidence following drainage and a meltwater inflow channel. The arrow matches that in Figure 7a. (c) Surface fractures that formed overnight near the NLBS field site during field missions, extending horizontally for tens or hundreds of meters. These cracks produced audible reports and ice motion that was observed by field team members.

such event pairs, with a standard deviation of 155 m. These values likely overestimated true uncertainties near the center of our network but underestimated them near the network edge. Figure 7a illustrates this error as a 155 m diameter uncertainty circle, centered at the drainage crack tip, which was near the center of our array.

Figure 8a shows the distribution in surface wave magnitudes (mean $M_S \sim 0.41$) for the events located in Figure 7, along with the distribution of seismic quality factors that were computed during magnitude regression (Figure 8b). While the greatest surface wave magnitude estimate (~3.3 magnitude units) appears intuitively too large, we found no visual problems with our waveform amplitude or period measurements and therefore did not censor our data. Further, the quality factors associated with these estimates (mean $Q \sim 45$) generally agree with the values that we estimated from the attenuation waveform model and implemented during location (mean $Q \sim 35$, Figure 4b). These values are higher than those reported by *Röösli et al.* [2014] but are consistent with values computed from an alpine Alaskan glacier [*Mikesell et al.*, 2012] and in ice of comparable depth upstream of Jakobshavn in Greenland [*Peters et al.*, 2012]. This consistency increases our confidence in the location and quality factor estimation methods. Figure 8c shows the corresponding estimates of deformation volume at the seismic source hypocenter (mean $\delta V = +0.85 \, \text{m}^3$). Assuming a fracture model, these volume changes are equivalent in scale to crack
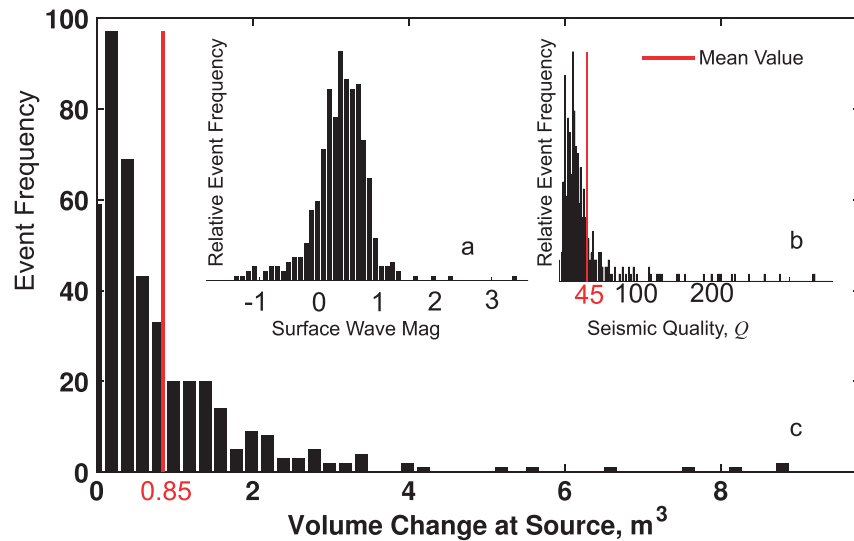
Figure 8. Histograms estimated from located icequake waveform amplitudes and epicentral solutions, with red vertical lines denoting mean values. (a) The distribution of surface wave magnitudes, computed from Rayleigh wave peak amplitudes and period. (b) The Rayleigh wave seismic quality factor (Q). Values are within range of those reported in glacial ice elsewhere [e.g., *Mikesell et al.*, 2012] and are consistent with the attenuation factors estimated through correlation (see Figure 4b). (c) The distribution for volumetric source growth, using a tensile fracture model. Values were determined by empirical relationships between surface wave and moment magnitudes scales. The cumulative growth in crack space from the 435 icequakes located here is $\sim 360\,m^3$.

face opening displacements of $\sim 1\,mm$ over fracture planes of $\sim 1000\,m^2$ area. Such features match field observations of newly formed surface cracks (e.g., Figure 7c) that appeared near site NLBS during early mornings over a 2–3 day period. The remaining, unlocated icequakes likely originated from cracks that were smaller than the sources that triggered the 435 located events shown in Figure 7a, since they produced lower SNR waveforms.

4.5. Relative Icequake Magnitude Analyses

We further analyzed the seismic magnitudes of the 435 located events to determine if (1) increased seismicity surrounding the lake drainage event or thereafter produced larger individual icequakes and (2) if multiplets produced successively larger icequakes that indicated increased source volume growth through crack plane extension. This analysis included assessing changes in magnitude with time duration surrounding the lake drainage, changes with epicentral distance from the drainage crack, and changes in magnitude for repeating icequakes over reemission time.

To first evaluate temporal changes, we compared the mean surface wave magnitudes of two different data sets of located events: icequakes occurring within 24 h of estimated drainage time on DOY 169 versus icequakes occurring ≥24 h before or after drainage time ($\overline{m}_{T1}$ versus $\overline{m}_{T2}$, Figure 9a). We then used a generalized likelihood ratio test [e.g., *Kay*, 1998, p. 187] to determine if these sample sets had similar statistical magnitude distributions at a 95% significance level. While we did not censor events by proximity from the crack tip, we did remove outlier influence on this test by implementing a modified sample variance estimator that subtracted the sample median, rather than the mean, from each sample. Our estimates gave statistically similar values of $\overline{m}_{T1} = 0.58$ and $\overline{m}_{T2} = 0.38$, with associated sample standard deviations of 0.47 and 0.53 (in magnitude units). Using these estimates, our likelihood test could not reject the hypothesis that the two sample sets had identical distributions, albeit with marginal significance (~96%). Therefore, we cannot confidently conclude that individual icequakes before the drainage were significantly larger in magnitude than those occurring after drainage.

We next evaluated spatial variability in event size by comparing surface wave magnitudes of icequakes with epicentral solutions ≤250 m from the crack axis to those with epicentral solutions ≥250 m from it ($\overline{m}_{D1}$ versus $\overline{m}_{D2}$). As before, we tested for distributional similarity between these two populations using a likelihood ratio
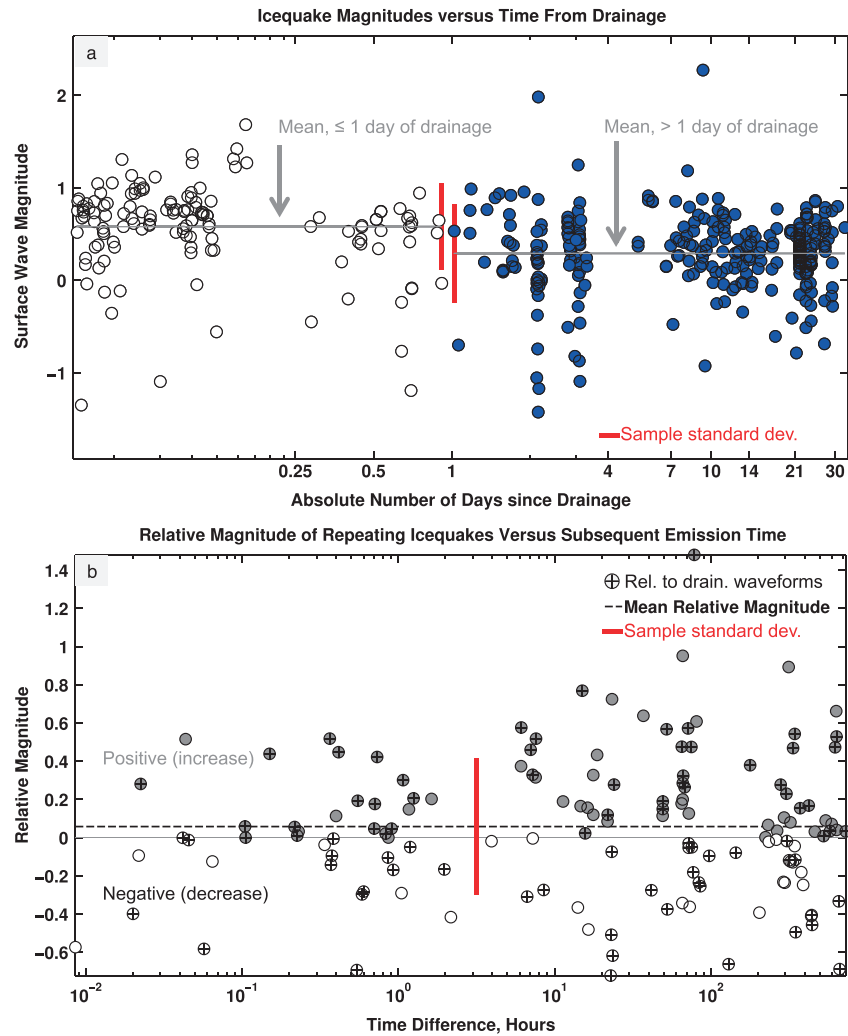
Figure 9. Comparisons between magnitudes of located events versus time since lake drainage and relative magnitudes of repeating icequakes (multiplets) versus time. (a) Icequake magnitudes versus time duration from drainage. The left, horizontal gray line shows the sample mean for surface magnitudes (white markers) occurring within 1 day of drainage. The right gray line shows the respective sample mean of surface wave magnitudes (blue markers) occurring ≥1 day before or after drainage. The red vertical bars illustrate the respective standard deviations for each sample and indicate statistically similar values between two event populations. (b) Relative magnitudes ΔM of icequakes (equation (7)) versus time for repeating events with similar hypocenters and waveforms, each with respect to an initial, reference event. Gray and white markers respectively indicate positive versus negative magnitude changes. The crossed markers indicate magnitudes measured relative to a reference waveform that occurred within 24 h of lake drainage. There is no statistically significant change in event size versus emission time that would indicate steadily increasing/decreasing source sizes.

test after accounting for outlier influence. We again found statistically similar mean magnitudes of $\overline{m}_{D1} = 0.34$ and $\overline{m}_{D2} = 0.38$ between the populations, and respective sample standard deviations of 0.33 and 0.42 (in magnitude units). Therefore, individual icequakes located near the drainage crack were not significantly larger compared to those located remotely from it.

Finally, we assessed any increased growth in fracture size by comparing relative magnitudes of icequakes within multiplets against event separation time. Using equation (7), we estimated magnitude differences ranging from ~10^{-4} (effectively identical events) to ~1.5 among 65 distinct clusters that contained between 2 and 13 similar events. Multiplets comprised ~62% of located drainage-associated events, ~40% of located postdrainage events, and ~32% of all available located events. We examined the significance of any magnitude changes within each of these sample sets by testing relative magnitudes as binomial
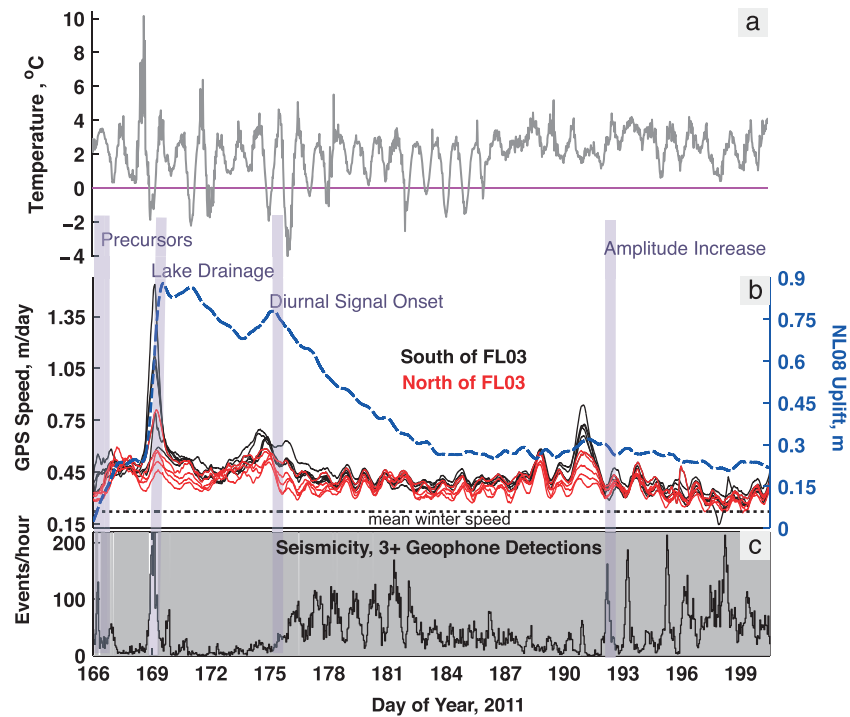
Figure 10. (a) Recorded air temperatures measured ~1 m above the ice surface, at the lakeshore. (b) Relative GPS elevation (blue) measured at site NL08 and ice speeds measured at sites with the same temporal coverage as the geophones (Figure 2). Colors correspond to Figure 1 and indicate sites north (red) or south (black) of FL03, and the dashed horizontal line indicates the average winter speed. (c) Icequake seismicity from Figure 3a; the vertical axis was truncated below the signal peak to increase the readability of the remaining record. Gray shading indicates where the hypothesized data distribution for the detection statistic fits within less than 20% RMS error. Seismicity and temperature in Figure 10a are generally anticorrelated, though phase lags vary. Purple bars across each plot indicate events interpreted from seismicity, and the x axis is ticked at midday. The transient features and spectral content of the GPS time series are discussed in section 4.8.

random variables, since this required the fewest assumptions on the data. Under this hypothesis, we assigned positive relative magnitudes as "successes" and computed their maximum likelihood probabilities and associated uncertainties. We thereby determined ~60% chance that multiplet magnitudes increased over time, among each population, but the uncertainty on this estimate was comparable to magnitude values and was therefore too large to be evidential (Figure 9b).

These results collectively indicate that fractures producing icequakes did not clearly change size with time surrounding lake drainage, with distance from the drainage crack, or at multiplet source locations indicating repeated growth of the same fracture.

4.6. General GPS Observations

Figure 10 illustrates 12 h moving averages of GPS speeds at each network receiver along with the daily averages in uplift history at site NL08. These time series are color coded according to latitude relative to site FL03 and are truncated between DOY 165 and 200 to only show data free of filtering end effects, which were also coincident with the seismic records. The site speeds maintained above winter values for effectively the whole record and show periods of interstation variability that appears temporally coincident with speedup events, as well as some local peaks in uplift. Other portions of these signals appear coherent across the network, with unclear diurnal variability. We therefore examined whether there was detectable diurnal variation in strain across our network by computing temporal averages over intrastation ranges in speed. Because it is difficult to measure diurnal patterns in GPS that are comparable to anticipated diurnal noise variability [*King et al.*, 2008], we evaluated day-scale changes in speed over the network by assuming that coincident noise variation was common to all receivers. This is reasonable because the GPS antennas were located well above the snow/ice surface and hence should
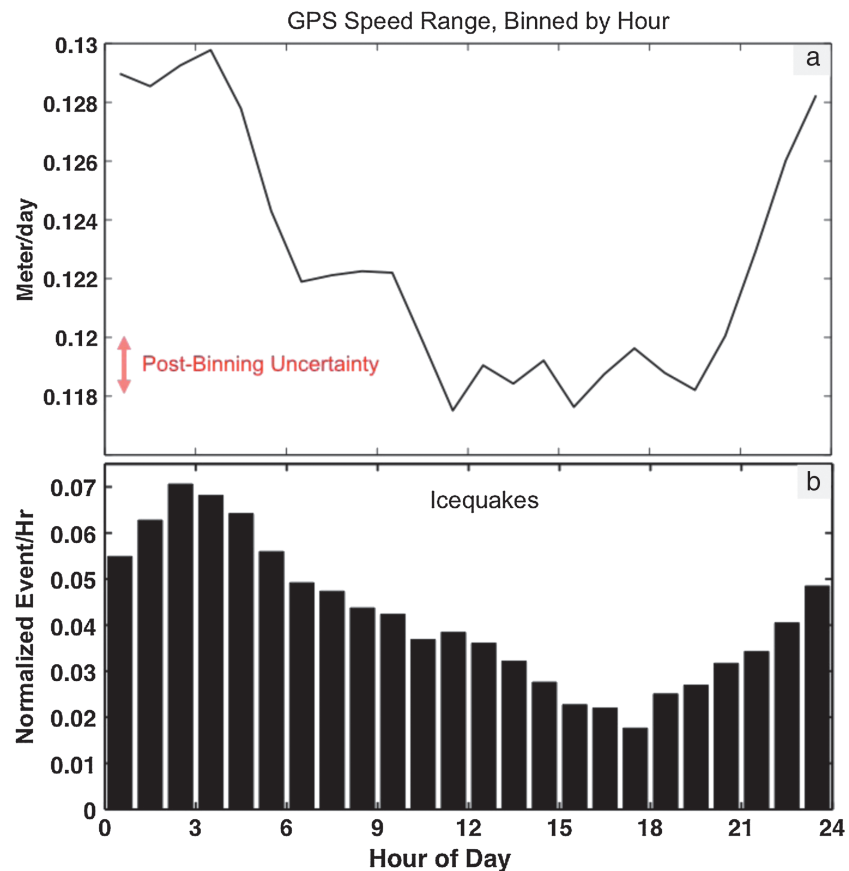
Figure 11. A comparison between the range in GPS speeds and icequake seismicity, averaged over 35 days and binned by hour (drainage event excluded). (a) Differences between the maximum and minimum GPS speeds (range) measured across the network and averaged by hour. The relative extrema indicate that network-wide spatial variability in speed was higher (on average) during early morning hours and lower during the day. Uncertainty after variance reduction from hourly binning is $\pm 2\,mm\,d^{-1}$. (b) The hourly seismicity from Figure 3b, shown for comparison. Data concurrent with the drainage are excluded from counts in each case.

be affected by a small multipath signal, the dominant site-specific GPS error. The remaining errors within the diurnal band originated from large-scale geophysical processes or satellite clock and orbit errors, both of which are common to all sites that we selected from our closely spaced GPS network [*Hoffman et al.*, 2011].

Under this assumption, we computed maximum differential speeds between distinct GPS sites and binned them by time of day as follows. We first compared the postprocessed speeds for each GPS receiver, at every time sample, by computing the difference between the maximum measured in-network GPS speed and the minimum measured in-network GPS speed (i.e., network range in speeds). This produced a time series for the intranetwork GPS speed range that we then binned by hour, for each individual day. The speed differences within each bin were then averaged over each day to compute a mean, hourly speed range over the relevant observation period; only dates following DOY 169 were used in this binning to avoid biasing the data with hours coincident with drainage-induced speedup.

This calculation proved insensitive to diurnal noise common to each GPS site, since the speed differencing removed the same noise trends. Our estimates therefore provided a variance-reduced computation of the mean peak speed gradient as it depends on hour of day. Figure 11 shows that these hourly binned averages are larger during late night/early morning hours and lowest during midday hours. We computed an uncertainty estimate for speed range in each bin using a $4\,m\,a^{-1}$ standard error for the 12 h filtered time series, which was further reduced by $1/\sqrt{30}$ through bin averaging over 30 (statistically independent)

days [*Hoffman et al.*, 2011]. Assuming that the cumulative position error was uniformly distributed among constituent days, these estimates provide a 0.2 cm d^{-1} uncertainty (~15% of the peak-to-peak difference), indicating that higher late evening/early morning speed gradients relative to midday are also physical.

4.7. Geophysical Response Leading Up To and Through Lake Drainage

To summarize ice sheet response for times <24 h after drainage, we compare the temperature record, icequake timing, epicentral distribution, and GPS history from DOY 165 to 170. The first notable event shown in our comparison between temperature, GPS speed, uplift, and seismicity (Figures 10a–10c) occurs 3 days prior to lake drainage (15 June, DOY 166), at which time elevated icequake activity accompanies uplift and an increase in surface speeds to 0.5 m/d or ~150% the average winter velocity. Epicentral solutions for icequakes located during this time (Figure 7) cluster south of the eventual drainage moulin (M1, purple arrow), proximal to GPS station NL08. Seismic activity subsequently decreases through DOY 168, while uplift ceases and speed remains relatively stable across the network. During this time, the highest air temperatures over the observation period were recorded and likely produced substantial meltwater input to the lake. These high temperatures were then followed by lake drainage at early local time on 18 June (DOY 169). This drainage coincided with rapid uplift rates at NL08 (0.6 m), an overall increase in both sliding speeds (~1.0 m/d) and their spatial variability, and a peak in icequake activity (up to 220 events/hour); because the exact timing of the initial drainage event is unknown, it is unclear if this peak included any precursory seismicity indicative of the impending hydrofracture. Located icequakes leading up to, and within 24 h after, hydrofracture predominantly clustered immediately west of M1 and likely indicate relatively high fracture density there. A substantial majority (~62%) of these located events were attributed to multiplets and almost certainly represent locations of active, repeated fracture propagation (discussed in section 4.5).

4.8. Postdrainage Geophysical Response

The day following drainage (DOY 170, Figures 9a–9c) is characterized by a dramatic decrease in seismicity and the return of ice velocities to predrainage values, at ~150% of the average winter speed. Associated uplift gradually subsides over the 2 weeks following drainage and is punctuated by a brief episode of renewed uplift on DOY 176 that accompanies increased speeds. A subsequent peak in this uplift coincides with a several-day period of increased seismicity that is marked by diurnally variable amplitudes. These amplitudes then decrease to ~50% of their mean value by DOY 183, as the decrease in the uplift levels off. Daily temperatures never drop below 0°C after DOY 185, likely resulting in sustained melt production. After this time, surface speeds show another local maximum near DOY 190, and icequake activity remains significantly diurnal (Figure 3b) but shares no obvious pointwise correlation with GPS motion. This activity also shows no clear pointwise relation with temperature data and is occasionally correlated with temperature peaks, while being anticorrelated other times. However, the average hourly seismicity (Figure 11) does exhibit an early morning maximum and midday minimum that is anticorrelated with average timing in peak melt production and, conversely, correlates with the nightly/early morning maximum and midday minimum in hourly GPS speed range. The seismicity also shows a longer-period component of elevated variability that is superimposed on the diurnal signal. This longer-period activity appears to comprise ~12 day patterns in which daily minimum icequake counts remain relatively steady compared with their peak-to-peak amplitudes. By DOY 200, geophone data are unreliable due to resonance of the instrument platform assembly, likely caused by melt out (see section 4.1).

Icequakes located over the postdrainage period generally cluster west of those occurring through DOY 169, roughly in the direction of ice flow (Figure 7a, blue markers). These sources are predominantly located farther from the crack, and nearer the zone of extensional strain located in the direction of a subglacial ridge to the northwest (see Figure 1). The region of enhanced seismicity also collocates with increased ice flow on the downstream side of the lake basin and in the direction of an expected migration path for meltwater supplied to the bed by moulins.

5. Discussion

Our first and most general result is that most detectable seismicity (~95%) in the lake basin and its immediate vicinity was caused by propagation of tensile or shear fractures within near-surface ice. These shallow fractures produced Rayleigh waves before and after drainage, indicating that detectable seismogenic deformation was

concentrated within one to two wavelengths (~330 m) of the ice surface. Average surface wave magnitudes of icequakes that we located ($M_S \sim 0.41$; Figure 8) are more than one half of a magnitude unit greater than those measured from Rayleigh waves triggered by surface cracking on an alpine glacier [*Mikesell et al.*, 2012], although some of our greatest absolute estimates (outliers) seem large and may be positively biased by unknown factors. From a crack source model, we estimate that these located events produced average deformation volumes of ~1 m^3 per icequake, equivalent to crack face opening displacements of ~1 mm over fracture planes of ~1000 m^2 area. Such dimensions are consistent with thin (millimeter wide) cracks extending over tens of meters that we observed during and immediately after lake drainage (Figure 7c).

This result is somewhat contrary to our initial assumptions. We expected postdrainage seismicity to dominantly involve basal seismicity once sliding, and ostensibly basal deformation, increased. Instead, body waveforms indicative of deeper icequakes comprised only ~5% of the icequake population at any time. Further, seismicity was most active at night when speed gradients peaked on average (Figure 11), but absolute speeds (and basal sliding) were at near minimum. We also concede, however, that basal seismicity is substantially less detectable on the Greenland Ice Sheet using our network. In typical noise conditions, basal icequakes must be at least two magnitude units or larger than surface icequakes of similar source dimensions to provide the same probability of detection. This diminished capability is mostly due to physical effects of propagation caused by anelastic attenuation and geometric spreading of deep-source body waves. This suggests that borehole stations may be required to detect icequakes of comparable magnitude to those measured here in the same noise environment.

5.1. Discussion: Lake Drainage

Supraglacial lake drainage coincides with a transient increase in surficial seismicity characterized by ~100 icequakes per hour with magnitudes that are statistically similar to those occurring more than a day before or after drainage. If precursory seismicity accompanies supraglacial lake drainage, it may occur over timescales that are too short to be clearly discriminated from the seismicity directly caused by hydrofracture or subsequent uplift. The relative absence of associated basal seismicity during drainage suggests either a lack of rapid (brittle) deformation at the ice bed interface during enhanced sliding or that basal events were not detected due to their relatively attenuated amplitudes within the recorded frequency band of our geophones. If drainage-generated basal seismicity is simply deficient relative to surficial events, such aseismic deformation could indicate the presence of a plastic till layer [e.g., *Bougamont et al.*, 2014] or that drainage-facilitated ice deformation is too plastic to seismically radiate within our geophone's pass band. If basal seismicity is produced from sliding, then deeper icequake signals may be detectable using broadband receivers capable of recording lower frequency (and longer-duration) waveforms. Such lower frequency waveforms (<1.8 Hz) are expected to undergo less attenuation and produce larger amplitudes (equation (4)) at wavelengths exceeding the ice sheet thickness (>1 km). In either case, a qualitatively similar dominance of surficial seismicity has also been observed from an alpine glacier during speedup triggered by an ice-marginal lake drainage [*Roux et al.*, 2010], and from a polythermal glacier with bed overdeepening [*Pomeroy et al.*, 2013], where sliding is known to occur. These results support a model in which transient melt-triggered sliding influences detectable seismicity primarily by promoting high-rate surface strains that cause ice fracture. It is also likely that basal seismicity at these glaciers is less detectable for the same physical reasons (attenuation and geometric spreading) that it is on the Greenland Ice Sheet.

While lake drainage greatly influenced emission rates of icequakes, it did not seem to detectably influence the relative size of individual icequake magnitudes. There was also was no major event corresponding to formation of the primary drainage crack. Specifically, the vertical hydrofracture was accommodated by a large number of small fractures instead of producing one major event. These observations suggest that seismic source size is not heavily controlled by transient uplift or speedup events coincident with drainage and that icequakes can relieve elevated ice column stresses rapidly enough that associated stress buildup does not trigger larger, less frequent icequakes. If magnitude changes do exist, they are too small relative to the variability of the absolute magnitudes to be easily observed. In this case, larger epicentral sample sizes are necessary to provide definitive conclusions. We suggest that detecting such differences requires an increased emphasis on assembling large data sets of icequake locations so that estimator variance of relative magnitudes is further reduced.

5.2. Discussion: Postdrainage

Diurnal variability in icequake activity persists throughout most of the post–lake drainage record, despite changes in background seismicity (Figures 3a and 3b). It is most pronounced after DOY 176, during the early morning hours and cannot be explained from fluctuations in background noise that reduce icequake detections (Figures 3c and 3d). These intervals of elevated activity are concurrent with low surface temperatures and meltwater production (Figure 10) and may reflect associated cycles in mechanical or thermal influence on ice deformation, as discussed below. Heightened activity during these hours is also consistent with field observations, in which audible cracking was heard near the NLBS site (Figure 1) and newly formed surface cracks were observed during early mornings over a 2–3 day period (Figure 7c). One source of surficial seismicity producing these signals may be local fluctuations in surface strain that induce the surface cracking. Decreased meltwater input to the bed during early mornings may increase spatial variability in basal traction as effective water pressure increases, so that patches of the bed and overlying ice come into contact. This could induce associated spatial variations in surface strain, at length scales shorter than resolvable with our GPS network (~2 ice thicknesses), which leads to seismogenic cracking. This model is also supported by the relatively small diurnal signal in both the GPS and seismicity between DOY 169 and 176. We suggest the diurnal variability in these signals is muted at this time because sufficient basal lubrication (as evident from the transient uplift signal) allowed sliding velocities to remain steadily high and less affected by daily melt input.

A link between surface seismicity and basal water input is also consistent with the shift in icequake locations shown in Figure 7a. Prior to drainage, it is likely that the bed received most local water input from the active southwest moulin (labeled M2 in Figure 1). After drainage, the water input through the lake moulin (M1) would have increased total water delivery to the region where seismic activity then increased. The addition of M1 north of M2 coincides with the northward shift of the mean predrainage and postdrainage epicentral points, which are shown by the white and blue markers, respectively, in Figure 7a. This would suggest that spatial differences in input location, and therefore basal lubrication, drive the high seismogenic strains.

Figure 11 gives additional support for the presence of a feedback between surface strain and seismicity. It illustrates the pointwise range in GPS speeds measured across the network, averaged into hour-of-day bins. Here, maximum speed differences (on average) peak with increases in average icequake activity during early morning hours. If this timing were unrelated to diurnal modulation (e.g., melt input), we would expect no significant hourly differences in peak speed gradients. Additionally, if this diurnal modulation is related to diurnal variability in meltwater input as we have proposed, then decreased melt input drives the measured spatial flow differences. This is again consistent with a model in which increases in spatially variable basal traction induce surface strains that open seismogenic tensile or shear cracks.

Finally, it is also possible that thermal effects may trigger some or all of the seismogenic surface fracturing. Prior observations elsewhere suggest that when strong temperature gradients cause elastic contraction in the shallow subsurface, they can induce tensile fracturing [*Lacroix*, 1980; C. Thurber, personal communication, 2012]. Alternatively, meltwater produced during warm hours in midday may refreeze at night within the cold subsurface in a process similar to the freeze-thaw cycles that break water-occupied porous rocks through heaving [*Murton et al.*, 2006]. Such experiments have demonstrated that pressures can greatly exceed the tensile strength of ice [*Dash et al.*, 2006]. Therefore, it seems plausible that thermal effects may trigger fracture propagation in the ice. We emphasize that these thermal effects may also act in parallel with spatial strain gradients to explain our observations.

5.3. Comparison With Regional Flow Patterns

The above-nominal winter values in surface speed (Figure 10b) indicate that surface ice may have been undergoing compressional or extensional flow during our observation period. Our local GPS network, however, does not provide a good estimation of the large-scale spatial variation in speed. We therefore compare our seismic locations with data for the prior years 2009 and 2010, which provide 11 day average estimates of the spatial variation in speed [*Joughin et al.*, 2013]; corresponding data from 2011 were not available for comparison. The data show substantial spatial variation in speed from one 11 day period to the next, which presumably occurs in addition to the day-to-day variability observed in the GPS data.
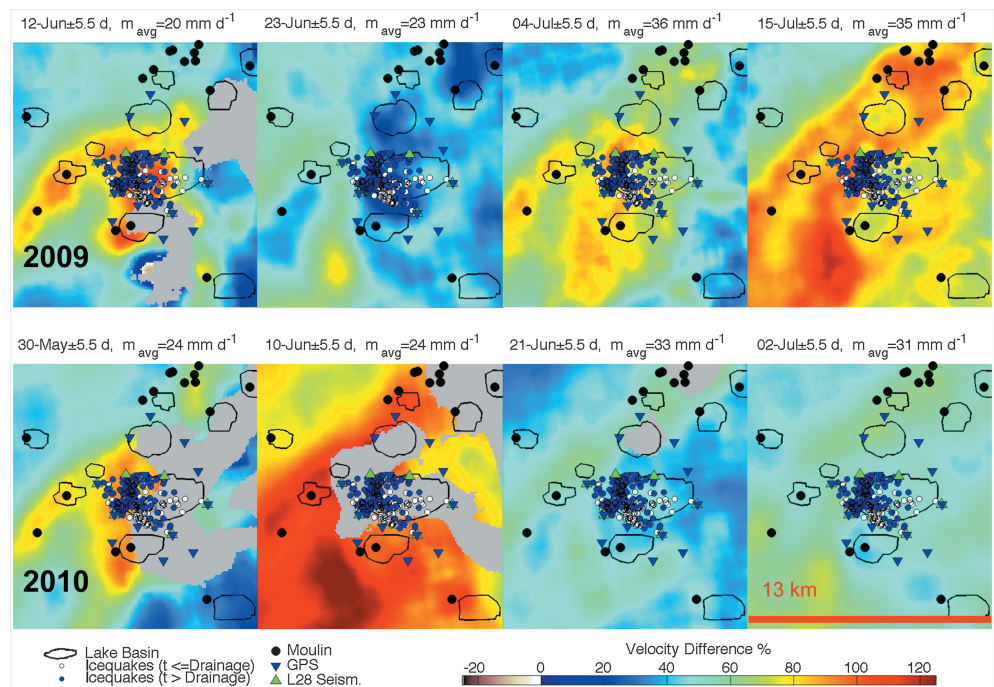
Figure 12. A comparison between velocity difference mosaics from *Joughin et al.* [2013] constructed using TerraSAR-X imagery from 2009 and 2010, superimposed with icequake epicenters and instrument coverage during the 2011 study period. Each 13 km × 14 km mosaic is indexed by the observation day, the uncertainty in the computation, and the estimated, average melt m_{avg} in millimeters per day. Coincident TerraSAR-X data from 2011 were unavailable. The leftmost panels illustrate a consistent pattern of enhanced velocity between the two years. Icequakes from Figure 7a are clustered densely along the regions of enhanced velocity present in the previous two years.

Although these maps of flow enhancement are from different years than our 2011 seismic data, they do reveal similar spatiotemporal patterns in the 2 years prior to seismic measurements, indicating similar variability is likely to have occurred in 2011. In fact, our epicentral estimates collocate with the two regions of relatively high ice speed in 2009 and 2010 (Figure 12), where extensional strain was likely high due to the comparatively slow upstream ice, and favorable for tensile or shear fracturing that produces icequakes. Furthermore, the data indicate the potential for relatively rapid (days) kilometer-scale transitions between tensile and compressive strain rates. Thus, summer speed enhancement may transiently produce regions of tensile strain within the lake basin where strains are compressive throughout the winter.

In addition, our seismic data show ~10–12 day periods in elevated activity that are likely indicative of enhanced surface fracture and is punctuated by periods of relatively low amplitude variability. These changes are also consistent with the temporal complexity documented by *Joughin et al.* [2013] in proximity to the same moulins shown in Figure 12. This TerraSAR-X imagery shows fluctuations of nearly 100% in surface speeds relative to winter values using 11 day averaged surface velocities. Our seismicity shares this variability and indicates associated speed variations may also occur over shorter periods. Although we had difficulty resolving such change in the GPS data, such variation may be occurring at length scales shorter than can be resolved with our GPS network ($<$ ~2 km, or 2 ice thicknesses). Alternatively, the TerraSAR-X image data provide comparatively high spatial resolution velocity maps of Greenland's ablation zone and may provide a more useful supplement to seismic array observations over comparative sensing apertures.

6. Conclusions

In this work, we used a network of geophones and GPS instruments to monitor ice sheet response before, during, and after the drainage of a kilometer-scale supraglacial lake in Greenland's ablation zone. We developed and implemented statistically robust detection methods that provided high-confidence estimates of icequake activity, location, seismic attenuation, and magnitudes for comparison with GPS

measurements of displacement and speed. We have demonstrated that surface-installed seismic networks provide evidence for melt season surface fracturing at a fine spatial resolution but may not detect deeper, brittle deformation near the ice bed interface of similar magnitudes.

Cumulatively, our observations indicate that the postdrainage spatial and temporal relationship between GPS speeds, temperature, and seismicity is complex in the lake-forming region. While icequake epicenters generally shift northwest from drainage-associated locations near the surface crack after lake drainage, subsequent seismicity shows an unclear relationship with time histories of GPS-derived speeds and uplift. Icequake magnitudes also show no significant change with drainage crack proximity or timing of drainage. Seismicity did, however, show heightened activity during early morning hours when the average range in GPS speeds peaked and the absolute speeds are at near minimum. There also is spatial coincidence with regions of repeatable, high surface speeds measured during previous years when data were available. This suggests that localized spatial variations in ice deformation, rather than sliding speed, may provide a better predictor for elevated seismic activity. Because surface speeds were almost uniformly above mean winter values network wide before drainage, the ice may have undergone significant extensional or compressional flow into the lake basin at that time. This evidence therefore suggests that icequakes triggered by tensile or shear fracturing may reflect stress modulations relative to an enhanced stress state; these stress modulations are initiated by changes in basal water pressures that are produced by lake drainage and differ from values predicted by temporally averaged flow characteristics. Further, our data indicate that seismicity is modulated by a diurnal forcing mechanism like meltwater input that may also control fine-scale variability in ice sheet flow. Thermal effects could additionally act in concert with this melt-forcing modulation to produce the observed diurnal variability in seismicity.

Our results indicate that the hydraulically triggered mechanisms controlling transient ice sheet response are still not completely understood on scales spanning one to several ice thicknesses. Further, the lack of detectable basal seismicity with and without enhanced sliding suggests either that instruments with a lower frequency pass band like broadband borehole instruments are required to detect such motion or that seismogenic stick-slip motion may not take place at the ice bed interface in the lake-forming region due to enhanced creep or till deformation.

Appendix A: Power Detectors

Icequakes must have sufficiently large magnitudes to generate ice motion that is detectable by the geophones within a network. Weaker or remote icequakes will produce smaller displacement amplitudes at the source that are statistically more difficult to distinguish from the expected amplitude of background noise recorded by geophones in the far field. To discriminate icequakes from such noise, a power detector evaluates a statistic z_k that is computed from a ratio of short-term and long-term averages (STA/LTA) of signal power [*Blandford*, 1974]. This statistic is derivable from a generalized likelihood ratio test [*Carmichael*, 2013] and is expressed at sample k, within a detection window containing statistically stationary noise, as

$$z_k = \left(\frac{1}{S} \sum_{n=k}^{n=k+S-1} \left(\frac{x_n}{\sigma} \right)^2 \right) \div \left(\frac{1}{L} \sum_{n=k-L+1}^{n=k} \left(\frac{x_n}{\sigma} \right)^2 \right) \qquad (A1)$$

where x_k is sample k of the observed seismogram, S is the leading, short window length in samples, L is the following long window length in samples, and σ is the standard deviation of background noise in the current detection window; while z_k is independent of σ, we maintain the notation for consistency with convention. Figure A1 shows z_k computed over 1800 s (middle) from the vertical component of NLBS (top) on DOY 181 with $S = 160$ samples and $L = 1000$ samples.

The statistic z_k has two distinct probability distribution functions, one applicable to the case of absent signal (a central F distribution) and one applicable to the case of present signal (a noncentral F distribution); their analytical forms are described in several places [e.g., *Kay*, 1998; *Carmichael*, 2013]. Deciding an icequake has occurred is equivalent to choosing the distribution function that explains the measured value of the STA/LTA statistic at a prescribed probability. The signal-present distribution is parameterized by a so-called
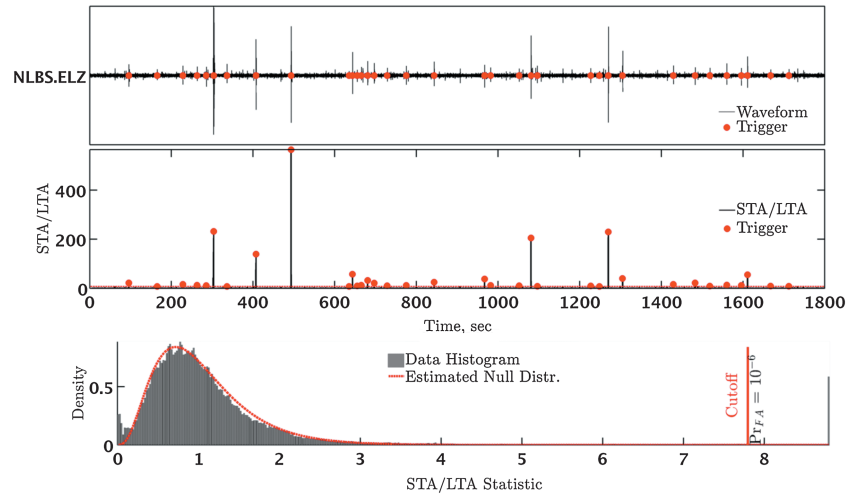
Figure A1. Power detector results as applied to 30 min of seismic data recorded at NLBS after local noon on DOY 181, which resulted in 43 single-station detections. (top) Vertical channel seismic data band pass filtered between 2.5 and 50 Hz. The red markers correspond to waveform detections and where the STA/LTA statistic exceeded the event declaration value. (middle) The STA/LTA statistic computed from the waveform data using a 0.8 s (160-sample) short-term window and a 5 s (1000-sample) long-term window; the red horizontal line shows the declaration threshold for a 10^{-6} false alarm rate (η, equation (A3)). (bottom) The histogram (gray) of the STA/LTA statistic, superimposed with the hypothesized null distribution (red, dashed curve). The shaping parameters for the predicted curve were estimated from N_1 and N_2 (equation (A4)), and the red vertical line indicates the threshold η from the middle panel; both estimates where made using the data shown here.

noncentrality parameter λ that is proportional to the waveform signal-to-noise ratio (SNR), which is zero for the signal-absent case. This parameter is defined by

$$\lambda = \sum_{k=1}^{S}\left(\frac{A_k}{\sigma}\right)^2 \tag{A2}$$

In equation (A2), A_k is the true (noise-free) waveform amplitude at sample k, which is related to the noise-contaminated data through $x_k = A_k + n_k$, where n_k is a sample of zero-mean background noise with standard deviation σ^2. Increasing values of λ (relative to zero) result in decreased overlap between the signal-present and signal-absent distributions, which raises the probability of correctly discriminating between noise and icequakes. A 0.95 probability of detecting an icequake at sample k that produces parameter λ is then obtained by integrating the probability density function over the detector threshold η consistent with a 10^{-6} detection probability:

$$0.95 = \int_{\eta}^{\infty} f_{Z_k}(z_k;\ \lambda,\ N_1,\ N_2)\mathrm{d}z_k$$

where

$$10^{-6} = \int_{\eta}^{\infty} f_{Z_k}(z_k;\ \lambda = 0,\ N_1,\ N_2)\mathrm{d}z_k \tag{A3}$$

In equation (A3), $f_{Z_k}(z_k;\ \lambda,\ N_1,\ N_2)$ is the signal-present F distribution, and $f_{Z_k}(z_k;\ \lambda = 0,\ N_1,\ N_2)$ is the signal-absent F distribution (Figure A1, bottom); each is parameterized by two degree-of-freedom parameters N_1 and N_2 that are respectively equal to S and L for white noise, but substantially less for real, temporally correlated noise. We estimate these parameters from our data using the mean and variance of the STA/LTA statistic:

$$E(z) = \frac{N_2}{N_2 - 2}$$
$$\mathrm{var}(z) = \frac{2N_2^2(N_1 + N_2 - 2)}{N_1(N_2 - 2)^2(N_2 - 4)} \tag{A4}$$

Using equation (A4), we computed the sample mean and sample variance in place of the true mean $E(z)$ and variance $\mathrm{var}(z)$ within each 1 h detection window using thousands of samples of z_k and then solved for N_1 and N_2.

Our degree-of-freedom estimates, combined with equation (A3), compose an implicit equation for λ that can be solved using the inverse cumulative distribution function for the noncentral F distribution (e.g., using MATLAB's ncfinv.m function). To estimate 95% threshold SNR parameters λ_{95}, we solved equation (A3) using hourly estimates of η, N_1, and N_2 (estimates denoted by hats):

$$\hat{\lambda}_{95} = \underset{\lambda}{\mathrm{argmin}} \left| 0.95 - \int_{\hat{\eta}}^{\infty} f_{Z_k}(z_k;\ \lambda,\ \hat{N}_1,\ \hat{N}_2)\, \mathrm{d}z_k \right| \tag{A5}$$

These results were used to assess the diurnality of icequake seismicity (Figure 3d) and compute threshold magnitudes by combining threshold estimates with simple source models (Figure 6; see also Appendix B). Other hypothesis tests and parameter estimates applied to icequake detection are documented by *Carmichael* [2013, Appendix A].

Appendix B: Seismic Signal Models

The time history for a velocity domain seismic waveform recorded by a geophone in the in far field (more than several wavelengths from the source) is expressible as:

$$A_k(t_k) = M_0 \left(\frac{F R_s^p}{4\pi r^n \rho c^3} \right) \cdot \Omega(t_k) \tag{B1}$$

where $A_k(t_k)$ is the waveform amplitude at time sample k, M_0 is the seismic moment, F is the free surface amplification factor, R_s^p is the seismic radiation pattern for phase p, r is the source-to-receiver distance, n is the phase exponent (1 for basal sources, 1/2 for surface sources), ρ is ice density, c is seismic wave speed, and $\Omega(t_k)$ is the seismic source-time function (a delta function here) at time sample t_k, after undergoing attenuation (by applying equation (4)) and convolution with the L-28 geophone instrument response function [e.g., *Oye et al.*, 2005]. To evaluate A_k for both surface and basal sources, we used the shear wave radiation pattern from a bed-parallel, double-couple source representing basal icequakes and the Rayleigh wave radiation pattern from a vertical-plane tensile crack representing surface icequakes. We then estimated R_s^p by averaging the root-mean-square (RMS) seismic radiation pattern of the largest predicted seismic phase for each source over an appropriate hypocenter-enclosing surface. We thereby computed $R_s^{\mathrm{Sh}} = \sqrt{\frac{2}{5}}$ using a focal sphere enclosing a basal source [*Aki and Richards*, 2002, p. 115] and $R_s^{\mathrm{Ray}} = \frac{\sqrt{26}}{12}$ using a focal cylinder enclosing a surficial crack; our computation of R_s^{Ray} is beyond the technical scope of this paper but can be derived using the Rayleigh wave Green's function solution [see *Aki and Richards*, 2002, p. 328]. We similarly computed free surface amplification values F for a basal source by applying the Zoeppritz equations with an incident SV wave [*Pujol*, 2003, section 6.5.3] and used $F = 1$ for a Rayleigh wave source.

With the coefficients F and R_s^p in equation (B1) defined, we express time-dependent threshold values for each source-specific scalar moment M_0 by combining waveform amplitude values of $A_k(t_k)$ with noncentrality parameter solutions defined by equation (A5). The threshold magnitudes for a basal shear source and Rayleigh wave surficial source are shown in Figure 6.

References

Agnew, D. C. (1997), NLOADF: A program for computing ocean-tide loading, *J. Geophys. Res.*, *102*(B3), 5109–5110, doi:10.1029/96JB03458.

Aki, K., and P. G. Richards (2002), *Quantitative Seismology*, vol. 2, Univ. Sci. Books, Mill Valley, Calif.

Allstadt, K., and S. D. Malone (2014), Swarms of repeating stick-slip icequakes triggered by snow loading at Mount Rainier volcano, *J. Geophys. Res. Earth Surf.*, *119*, 1180–1203, doi:10.1002/2014JF003086.

Andrews, L. C., G. A. Catania, M. J. Hoffman, J. D. Gulley, M. P. Luthi, C. Ryser, R. L. Hawley, and T. A. Neumann (2014), Direct observations of evolving subglacial drainage beneath the Greenland Ice Sheet, *Nature*, *514*(7520), 80–83.

Bartholomew, I., P. Nienow, A. Sole, D. Mair, T. Cowton, M. A. King, and S. Palmer (2011a), Seasonal variations in Greenland Ice Sheet motion: Inland extent and behaviour at higher elevations, *Earth Planet. Sci. Lett.*, *307*, 271–278.

Bartholomew, I., P. Nienow, A. Sole, D. Mair, T. Cowton, S. Palmer, and J. Wadham (2011b), Supraglacial forcing of subglacial drainage in the ablation zone of the Greenland Ice-Sheet, *Geophys. Res. Lett.*, *38*, L08502, doi:10.1029/2011GL047063.

Bertiger, W., S. Desai, B. Haines, N. Harvey, A. Moore, S. Owen, and J. Weiss (2010), Single receiver phase ambiguity resolution with GPS data, *J. Geod.*, *84*(5), 327–337, doi:10.1007/s00190-010-0371-9.

Blandford, R. R. (1974), An automatic event detector at the Tonto Forest Seismic Observatory, *Geophysics*, *39*(5), 633–643.

Boehm, J., B. Werl, and H. Schuh (2006), Troposphere mapping functions for GPS and very long baseline interferometry from European Centre for Medium-Range Weather Forecasts operational analysis data, *J. Geophys. Res.*, *111*, B02406, doi:10.1029/2005JB003629.

Bougamont, M. A., P. Christoffersen, A. L. Hubbard, A. A. Fitzpatrick, S. H. Doyle, and S. P. Carter (2014), Sensitive response of the Greenland Ice Sheet to surface melt drainage over a soft bed, *Nat. Commun.*, *5*, 5052.

Bowers, D., and J. A. Hudson (1999), Defining the scalar moment of a seismic source with a general moment tensor, *Bull. Seismol. Soc. Am.*, *89*(5), 1390–1394.

Canassy, P. D., J. Faillettaz, F. Walter, and M. Huss (2012), Seismic activity and surface motion of a steep temperate glacier: A study on Triftgletscher, Switzerland, *J. Glaciol.*, *58*(209), 513–528, doi:10.3189/2012JoG11J104.

Carmichael, J. D. (2013), Melt-triggered seismic response in hydraulically-active polar ice: Observations and methods, PhD thesis, Univ. of Wash., Seattle. [Available at http://hdl.handle.net/1773/25007.]

Carmichael, J. D., E. C. Pettit, M. Hoffman, A. Fountain, and B. Hallet (2012), Seismic multiplet response triggered by melt at Blood Falls, Taylor Glacier, Antarctica, *J. Geophys. Res.*, *117*, F03004, doi:10.1029/2011JF002221.

Chael, E. P. (1997), An automated Rayleigh-wave detection algorithm, *Bull. Seismol. Soc. Am.*, *87*(1), 157–163.

Dash, J. G., A. W. Rempel, and J. S. Wettlaufer (2006), The physics of premelted ice and its geophysical consequences, *Rev. Mod. Phys.*, *78*(3), 695–741, doi:10.1103/RevModPhys.78.695.

Das, S. B., I. Joughin, M. D. Behn, I. M. Howat, M. A. King, D. Lizarralde, and M. P. Bhatia (2008), Fracture propagation to the base of the Greenland Ice Sheet during supraglacial lake drainage, *Science*, *320*(5877), 778–781, doi:10.1126/science.1153360.

Das, S. B., M. D. Behn, and I. R. Joughin (2011), Modes of supraglacial lake drainage and dynamic ice sheet response, AGU, Fall Meeting 2011.

Doyle, S. H., A. L. Hubbard, C. F. Dow, G. A. Jones, A. Fitzpatrick, A. Gusmeroli, B. Kulessa, K. Lindback, R. Pettersson, and J. E. Box (2013), Ice tectonic deformation during the rapid in situ drainage of a supraglacial lake on the Greenland Ice Sheet, *Cryosphere*, *7*(1), 129–140, doi:10.5194/tc-7-129-2013.

Doyle, S. H., A. Hubbard, A. A. W. Fitzpatrick, D. van As, A. B. Mikkelsen, R. Pettersson, and B. Hubbard (2014), Persistent flow acceleration within the interior of the Greenland Ice-Sheet, *Geophys. Res. Lett.*, *41*, 899–905, doi:10.1002/2013GL058933.

Egbert, G. D., S. Y. Erofeeva, S. C. Han, S. B. Luthcke, and R. D. Ray (2009), Assimilation of GRACE tide solutions into a numerical hydrodynamic inverse model, *Geophys. Res. Lett.*, *36*, L20609, doi:10.1029/2009GL040376.

Fitzpatrick, A. A. W., A. L. Hubbard, J. E. Box, D. J. Quincey, D. van As, A. P. B. Mikkelsen, S. H. Doyle, C. F. Dow, B. Hasholt, and G. A. Jones (2014), A decade (2002–2012) of supraglacial lake volume estimates across Russell Glacier, West Greenland, *Cryosphere*, *8*(1), 107–121.

Futterman, W. I. (1962), Dispersive body waves, *J. Geophys. Res.*, *67*(13), 5279–5291, doi:10.1029/JZ067i013p05279.

Gibbons, S. J., and F. Ringdal (2006), The detection of low magnitude seismic events using array-based waveform correlation, *Geophys. J. Int.*, *165*(1), 149–166, doi:10.1111/j.1365-246X.2006.02865.x.

Gibowicz, S. J., and A. Kijko (1994), *An Introduction to Mining Seismology*, Academic Press, San Diego, Calif.

Gusmeroli, A., R. A. Clark, T. Murray, A. D. Booth, B. Kulessa, and B. E. Barrett (2010), Seismic wave attenuation in the uppermost glacier ice of Storglaciaren, Sweden, *J. Glaciol.*, *56*(196), 249–256.

Harris, D. B. (1989), Characterizing source regions with signal subspace methods: Theory and computational methods (No. UCID-21848). Lawrence Livermore National Lab., Calif.

Harris, D. B. (1991), A waveform correlation method for identifying quarry explosions, *Bull. Seismol. Soc. Am.*, *81*(6), 2395–2418.

Helmstetter, A., B. Nicolas, P. Comon, and M. Gay (2015), Basal icequakes recorded beneath an Alpine glacier (Glacier d'Argentière, Mont Blanc, France): Evidence for stick-slip motion?, *J. Geophys. Res. Earth Surf.*, *120*, doi:10.1002/2014JF003288.

Hoffman, M. J., G. A. Catania, T. A. Neumann, L. C. Andrews, and J. A. Rumrill (2011), Links between acceleration, melting, and supraglacial lake drainage of the western Greenland Ice Sheet, *J. Geophys. Res.*, *116*, F04035, doi:10.1029/2010JF001934.

Jones, G. A., B. Kulessa, S. H. Doyle, C. F. Dow, and A. Hubbard (2013), An automated approach to the location of icequakes using seismic waveform amplitudes, *Ann. Glaciol.*, *54*(64), 1–9.

Joughin, I., S. B. Das, M. A. King, B. E. Smith, I. M. Howat, and T. Moon (2008), Seasonal speedup along the western flank of the Greenland Ice Sheet, *Science*, *320*(5877), 781–783, doi:10.1126/science.1153439.

Joughin, I., S. B. Das, G. E. Flowers, M. D. Behn, R. B. Alley, M. A. King, B. E. Smith, J. Bamber, M. R. van den Broeke, and J. H. van Angelen (2013), Influence of ice-sheet geometry and supraglacial lakes on seasonal ice-flow variability, *Cryosphere*, *7*, 1185–1192.

Kay, S. M. (1998), *Fundamentals of Statistical Signal Processing: Volume II*, Prentice-Hall PTR, Englewood Cliffs, N. J.

King, M., and S. Aoki (2003), Tidal observations on floating ice using a single GPS receiver, *Geophys. Res. Lett.*, *30*(3, 1138), doi:10.1029/2002GL016182.

King, M. A., C. S. Watson, N. T. Penna, and P. J. Clarke (2008), Subdaily signals in GPS observations and their effect at semiannual and annual periods, *Geophys. Res. Lett.*, *35*, L03302, doi:10.1029/2007GL032252.

Krawczynski, M. J., M. D. Behn, S. B. Das, and I. Joughin (2009), Constraints on the lake volume required for hydro-fracture through ice sheets, *Geophys. Res. Lett.*, *36*, L10501, doi:10.1029/2008GL036765.

Kubokawa, T., C. P. Robert, and A. K. M. E. Saleh (1993), Estimation of noncentrality parameters, *Can. J. Stat.*, *21*, 45–57, doi:10.2307/3315657.

Lacroix, A. V. (1980), A short note on cryoseisms, *Seismol. Res. Lett.*, *51*(1), 15–21.

Leeson, A. A., A. Shepherd, K. Briggs, I. Howat, X. Fettweis, M. Morlighem, and E. Rignot (2015), Supraglacial lakes on the Greenland ice-sheet advance inland under warming climate, *Nat. Clim. Change*, *5*(1), 51–55.

Liang, Y. L., W. Colgan, Q. Lv, K. Steffen, W. Abdalati, J. Stroeve, D. Gallaher, and N. Bayou (2012), A decadal investigation of supraglacial lakes in West Greenland using a fully automatic detection and tracking algorithm, *Remote Sens. Environ.*, *123*, 127–138.

Mikesell, T. D., K. van Wijk, M. M. Haney, J. H. Bradford, H. P. Marshall, and J. T. Harper (2012), Monitoring glacier surface seismicity in time and space using Rayleigh waves, *J. Geophys. Res.*, *117*, F02020, doi:10.1029/2011JF002259.

Moriya, H., H. Niitsuma, and R. Baria (2003), Multiplet-clustering analysis reveals structural details within the seismic cloud at the Soultz geothermal field, France, *Bull. Seismol. Soc. Am.*, *93*(4), 1606–1620, doi:10.1785/0120020072.

Müller, G. (2001), Volume changes of seismic sources from moment tensors, *Bull. Seismol. Soc. Am.*, *91*(4), 880–884.

Murton, J. B., R. Peterson, and J. Ozouf (2006), Bedrock fracture by ice segregation in cold regions, *Science*, *314*(5802), 1127–1129, doi:10.1126/science.1132127.

Oye, V., H. Bungum, and M. Roth (2005), Source parameters and scaling relations for mining-related seismicity within the Pyhäsalmi ore mine, Finland, *Bull. Seismol. Soc. Am.*, *95*(3), 1011–1026.

Palmer, S., A. Shepherd, P. Nienow, and I. Joughin (2011), Seasonal speedup of the Greenland Ice Sheet linked to routing of surface water, *Earth Planet. Sci. Lett.*, *302*(3–4), 423–428, doi:10.1016/j.epsl.2010.12.037.

Peters, L. E., S. Anandakrishnan, R. B. Alley, and D. E. Voigt (2012), Seismic attenuation in glacial ice: A proxy for englacial temperature, *J. Geophys. Res.*, *117*, F02008, doi:10.1029/2011JF002201.

Petit, G., and B. Luzum (2010), IERS Conventions, Rep., ISBN 3-89888-989-6, 179 pp, Frankfurt am Main.

Poinar, K., I. Joughin, S. B. Das, M. D. Behn, J. T. M. Lenaerts, and M. R. van den Broeke (2015), Limits to future expansion of surface-melt-enhanced ice flow into the interior of western Greenland, *Geophys. Res. Lett.*, *42*, 1800–1807, doi:10.1002/2015GL063192.

Pomeroy, J., A. Brisbourne, J. Evans, and D. Graham (2013), The search for seismic signatures of movement at the glacier bed in a polythermal valley glacier, *Ann. Glaciol.*, *54*(64), 149–156, doi:10.3189/2013AoG64A203.

Pujol, J. (2003), *Elastic Wave Propagation and Generation in Seismology*, Cambridge Univ. Press, Cambridge.

Ringdal, F., and T. Kværna (1992), Continuous seismic threshold monitoring, *Geophys. J. Int.*, *111*(3), 505–514.

Röösli, C., F. Walter, S. Husen, L. C. Andrews, M. P. Luthi, G. A. Catania, and E. Kissling (2014), Sustained seismic tremors and icequakes detected in the ablation zone of the Greenland Ice-Sheet, *J. Glaciol.*, *60*(221), 563–575.

Roux, P., F. Walter, P. Riesen, S. Sugiyama, and M. Funk (2010), Observation of surface seismic activity changes of an Alpine glacier during a glacier-dammed lake outburst, *J. Geophys. Res.*, *115*, F03014, doi:10.1029/2009JF001535.

Ryser, C., M. P. Luthi, L. C. Andrews, G. A. Catania, M. Funk, R. L. Hawley, M. J. Hoffman, and T. A. Neumann (2014), Caterpillar-like ice motion in the ablation zone of the Greenland ice-sheet, *J. Geophys. Res. Earth Surf.*, *199*, 2258–2271, doi:10.1002/2013JF003067.

Schaff, D. P., and P. G. Richards (2014), Improvements in magnitude precision, using the statistics of relative amplitudes measured by cross correlation, *Geophys. J. Int.*, *197*(1), 335–350, doi:10.1093/gji/ggt433.

Schoof, C. (2010), Ice-sheet acceleration driven by melt supply variability, *Nature*, *468*(7325), 803–806, doi:10.1038/nature09618.

Selmes, N., T. Murray, and T. D. James (2011), Fast draining lakes on the Greenland Ice Sheet, *Geophys. Res. Lett.*, *38*, L15501, doi:10.1029/2011GL047872.

Shepherd, A., A. Hubbard, P. Nienow, M. King, M. McMillan, and I. Joughin (2009), Greenland ice-sheet motion coupled with daily melting in late summer, *Geophys. Res. Lett.*, *36*, L01501, doi:10.1029/2008GL035758.

Stuart, G., T. Murray, A. Brisbourne, P. Styles, and S. Toon (2005), Seismic emissions from a surging glacier: Bakaninbreen, Svalbard, *Ann. Glaciol.*, *42*, 151–157, doi:10.3189/172756405781812538.

Sundal, A. V., A. Shepherd, P. Nienow, E. Hanna, S. Palmer, and P. Huybrechts (2009), Evolution of supra-glacial lakes across the Greenland Ice Sheet, *Remote Sens. Environ.*, *113*(10), 2164–2171, doi:10.1016/j.rse.2009.05.018.

Tedesco, M., I. C. Willis, M. J. Hoffman, A. F. Banwell, P. Alexander, and N. S. Arnold (2013), Ice dynamic response to two modes of surface lake drainage on the Greenland Ice-Sheet, *Environ. Res. Lett.*, *8*(3), 034007.

Thelen, W. A., K. Allstadt, S. De Angelis, S. D. Malone, S. C. Moran, and J. Vidale (2013), Shallow repeating seismic events under an alpine glacier at Mount Rainier, Washington, USA, *J. Glaciol.*, *59*(214), 345–356, doi:10.3189/2013JoG12J111.

Walter, F., N. Deichmann, and M. Funk (2008), Basal icequakes during changing subglacial water pressures beneath Gornergletscher, Switzerland, *J. Glaciol.*, *54*(186), 511–521, doi:10.3189/002214308785837110.

Walter, F., J. F. Clinton, N. Deichmann, D. S. Dreger, S. E. Minson, and M. Funk (2009), Moment tensor inversions of icequakes on Gornergletscher, Switzerland, *Bull. Seismol. Soc. Am.*, *99*(2A), 852–870, doi:10.1785/0120080110.

Weichecki-Vergara, S., H. L. Gray, and W. A. Woodward (2001), Statistical development in support of CTBT monitoring, *Tech. Rep. DTRA-TR-00-22*, Southern Methodist Univ., Dallas, Tex.

Zumberge, J. F., M. B. Heflin, D. C. Jefferson, M. M. Watkins, and F. H. Webb (1997), Precise point positioning for the efficient and robust analysis of GPS data from large networks, *J. Geophys. Res.*, *102*(B3), 5005–5017, doi:10.1029/96JB03860.